

GLAMOUR: GRAPH LEARNING OVER MACROMOLECULE REPRESENTATIONS

Somesh Mohapatra, Joyce An & Rafael Gómez-Bombarelli*

Department of Materials Science and Engineering

Massachusetts Institute of Technology

Cambridge, MA 02139, USA

{someshm, joycean, rafagb}@mit.edu

ABSTRACT

The near-infinite chemical diversity of natural and artificial macromolecules arises from the vast range of possible component monomers, linkages, and polymers topologies. This enormous macromolecular diversity contributes to the ubiquity and indispensability of macromolecules but hinders the development of general machine learning methods with macromolecules as input. To address this, we developed GLAMOUR, a framework for chemistry-informed graph representation of macromolecules that enables quantifying structural similarity, and interpretable supervised learning for macromolecules.

1 INTRODUCTION

Machine learning (ML) applications to individual macromolecule classes, such as proteins, have been very successful but typically rely on sequence-based representations that effectively capture structures with linear architectures (Schissel et al., 2021; Alley et al., 2019). However, these methods do not extend to macromolecules with complex topologies, such as glycans and biohybrid sequence-defined polymers, which exhibit non-linear structure and higher levels of monomer and linkage diversity. Graphs are a natural and more general macromolecule representation, with nodes representing monomers and edges representing connecting bonds. ML over graph representations has achieved state-of-the-art results across several fields (Hamilton et al., 2017) (see Section A for a survey of the field) and in chemistry and life sciences, graph neural networks (GNNs) have become the modern workhorse for molecular property prediction (Yang et al., 2019; Jin et al., 2020). Attribution methods are compatible with GNNs to highlight how input features are relevant to model predictions of target properties, such as molecular olfactory descriptors (Sanchez-Lengeling et al., 2020; 2019).

In this work, we developed a graph representation for macromolecules. The representation generalizes ideas of macromolecule similarity from sequence alignment to structural similarity between complex topologies. Using chemical similarity between monomers through cheminformatic fingerprints and exact graph edit distances (GED) or graph kernels to compare topologies, it allows for quantification of the chemical and structural similarity of two arbitrary macromolecule topologies. Further, the representation was coupled to supervised GNN models to learn structure-property relationships in glycans and anti-microbial peptides. The graph representation handles linear, branched and cyclic topologies along with any monomer composition. Attribution methods highlight the regions of the macromolecules and the substructures within the monomers that are most responsible for the predicted properties.

2 RESULTS AND DISCUSSION

We developed a generalized text file system to convert a macromolecule structure into a machine-readable format (Figure 1A, Section C). The text file has three sections – SMILES, MONOMERS, and BONDS, inspired by the PDB file format (Berman, 2000). Under SMILES, monomer and bond

*Corresponding author: rafagb@mit.edu.

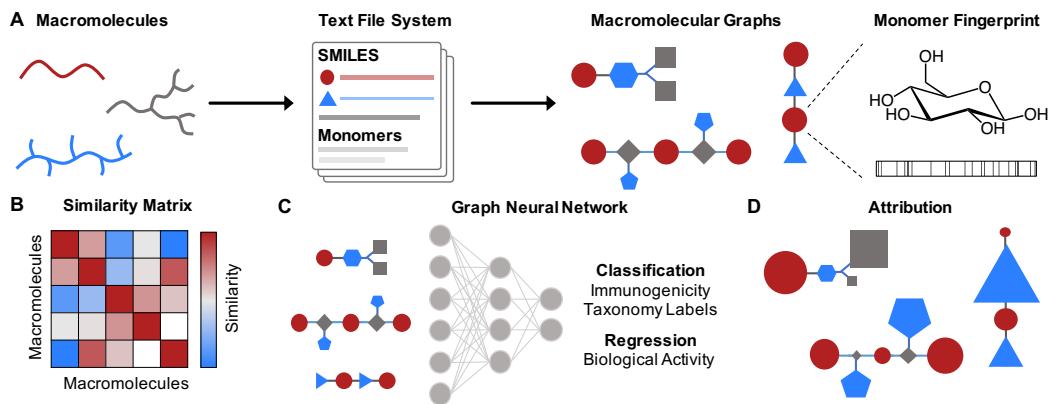


Figure 1: **Macromolecules represented as graphs enable similarity computation and interpretable machine learning.** **A.** Macromolecular structures are converted into text files. The text files are parsed into network graphs, where monomers are nodes and bonds are edges. Each text file enumerates SMILES for monomers and bonds, node indices corresponding to monomers, and pairs of node indices for bonds. Node and edge attributes are fingerprints of respective molecules. **B.** Pair-wise similarity matrix obtained for the library of macromolecules, and dimensionality reduction followed by clustering of similarity vectors corresponding to each macromolecule. **C.** Graph neural networks learn over macromolecule graphs for various tasks. **D.** Graph attribution provides insight into the model’s decision-making process by highlighting the relative importance of different nodes/monomers (denoted as node size) in making a specific prediction.

names followed by the stereochemical SMILES are noted. MONOMERS enumerates indices of all nodes numbered from 1 to n , where n is the total number of monomers, followed by the monomer names. Similarly, BONDS lists indices of connections between monomer indices, followed by bond names. In this way, we are able to incorporate complexity from the level of individual atoms to the full macromolecular structure.

In our experiments, the macromolecules were then processed as NetworkX graphs (Hagberg et al., 2008), with monomers as nodes and bonds as edges (Section D). In line with earlier work where fingerprint-based monomer representations worked effectively for macromolecule property prediction, the monomer and bond molecules were featurized using standard Extended Connectivity FingerPrints (Schissel et al., 2021). The fingerprints capture the atomic connectivity of the monomer/bond molecule as a series of bits using circular atom neighborhoods, for each constituent node or edge of the macromolecule graph. This representation enables the encoding of the raw chain connectivity of macromolecules with explicit featurization of the stereochemistry and topology. Moreover, it provides a single framework to represent both natural and synthetic, linear and non-linear macromolecules.

To compute the similarity between 2 or more macromolecule graphs, we used GED and graph kernel (Figure 1B, Section E). GED (Abu-Aisheh et al., 2015) computes the similarity between two graphs by assigning node and edge substitution scores, similar to local sequence alignment methods, such as BLAST (Altschul et al., 1990). Instead of evolutionary statistics-based substitution matrices like BLOSUM62, we used Tanimoto chemical similarity matrices that compute the similarity between molecular fingerprints. Tanimoto similarity also extends to unnatural monomers. Since computing exact graph edit distances is an NP-hard problem, we used propagation attribute graph kernels to obtain approximate similarity matrices for large datasets (Neumann et al., 2016; Siglidis et al., 2020). This graph kernel captures local monomer node information and propagates this information along the bond edges, making it an ideal choice for macromolecule graphs. We have demonstrated the similarity computation for a linear glycan with six additional glycans of different topology and/or monomer chemistry, as well as with itself, using Tanimoto chemical similarity matrix (Figure 2A, B).

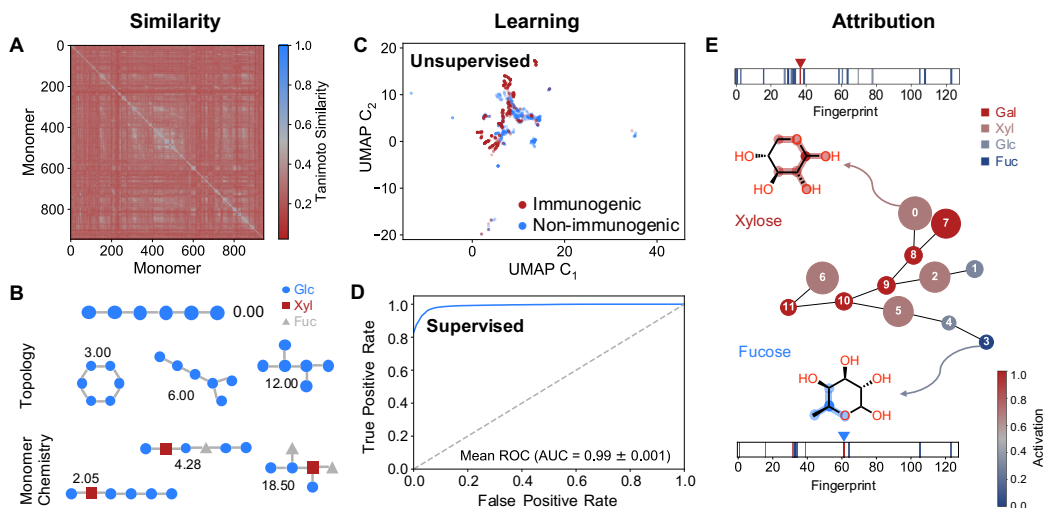


Figure 2: Analysis using GLAMOUR provides deeper insights into immunogenicity of glycans. **A.** Pairwise chemical similarity between glycan monomers using Tanimoto distance on ECFP fingerprints is typically low. **B.** Similarities between a linear glycan consisting of six glucose monomers with itself and six additional glycans with modified topology and monomer chemistry were computed using exact graph edit distances, combined with the Tanimoto substitution matrices (A). **C.** 2-component UMAP over the similarity matrix, colored by immunogenicity, for 1313 glycans with immunogenicity labels. **D.** Mean ROC-AUC curve for classification of immunogenic and non-immunogenic glycans, averaged across all 25 Attentive FP models (5 random seeds, with top 5 sets of hyperparameters), with the standard deviation shaded in light blue too insignificant to be visible in the graph. **E.** Attribution analysis using Attentive FP model architecture and integrated gradients attribution method for a representative glycan shows that xylose (Xyl) contributes the most to immunogenicity. In xylose, the substructure centered on the anomeric carbon, C1, is shown to be the key contributor. A similar substructure analysis has been shown for fucose. In the glycan graph, the size of the node corresponds to the importance, and the color corresponds to the monomer. In the fingerprint, only the indices with positive contribution to immunogenicity have been visualized, with the color corresponding to the normalized importance

Because quantifying graph similarity enables unsupervised learning over similarities rather than raw features, we used dimensionality reduction methods, such as uniform manifold approximation and projection (UMAP) (McInnes et al., 2018) and t-stochastic neighbor embeddings (t-SNE) (Van Der Maaten & Hinton, 2008), over the similarity matrices for unsupervised learning (Section F). For glycans with immunogenicity labels, we observed that the non-immunogenic and immunogenic glycans are in nearly distinct regions (Figure 2C).

For supervised learning, we trained five different GNN model architectures to classify glycans by immunogenicity and taxonomy levels, and predict the anti-microbial activity of peptides (Section G). Each model architecture was trained over fingerprint and one-hot node and edge attributes on 60%, validated on 20%, and tested on held-out 20% data set, all determined via random splits. Hyperparameter optimization was carried out for 1000 iterations using SigOpt (Clark & Hayes, 2019). To report final metrics on validation and test datasets, for each model architecture, we averaged values obtained from 25 individual models – top 5 hyperparameter sets, each trained with 5 random seeds. For glycans, our models outperformed metrics for classification for four out of eight tasks and achieved comparable results for the rest four, against results reported in the literature (Figure 2D, Table A.5) (Burkholz et al., 2021).

Attribution analysis on the pre-trained models finds features – both nodes and substructures – that are key to the model’s decision-making (Section H). To avoid spurious hypotheses (McCloskey et al., 2019) that may occur in NN attribution on molecular models, we chose the combination of GNN architecture and attribution method, in this case Attentive FP - integrated gradients, that pro-

duced the most consistent results across all immunogenic glycans over 25 replicates (Figure A.45). N-glycolylneuraminic acid, xylose, and fucose were found to be the key monomers responsible for immunogenicity, consistent with experimental findings due to the low prevalence of these monomers in human glycans (Planinc et al., 2016) (Table A.7). For a representative glycan, we observed that xylose, followed by galactin, were the monomers that contributed most significantly to immunogenicity (Figure 2E). In addition to the importance of individual nodes, attribution identifies the critical substructures in the monomers that contributed most to immunogenicity, such as the substructure centered on the anomeric carbon of xylose. These critical features help understand the fundamental structure-function relationships that underpin immunogenicity, postulate very explicit hypotheses that can be validated in the lab, and may help in further design of immunogenic or non-immunogenic scaffolds.

3 CONCLUSION

GLAMOUR provides a generalized method for representing macromolecules as hierarchical graphs with molecular fingerprints to capture chemical information which can be used to compute structural similarity between macromolecules with different composition and topology, and perform unsupervised and supervised learning. The unsupervised learning enables visualization of the complex landscape of different classes of macromolecules and understanding of the subtle differences between similar macromolecules. The attribution analysis helps in cracking open the black-box of supervised GNN models, which in turn can help elucidate fundamental design principles of otherwise opaque structure-property relationships and assist with hypothesis generation for future experimental studies. The codebase and data sets have been open-sourced (Mohapatra, 2021). We therefore expect that this toolkit will be used by both experimentalists and computational practitioners in chemistry, biology and materials science for a variety of macromolecule property prediction tasks, ultimately driving the design of improved macromolecules.

DATA AVAILABILITY

Data used for training of the model is available at <https://github.com/learningmattermit/GLAMOUR>, and archived in the Zenodo repository (Mohapatra, 2021).

CODE AVAILABILITY

All the code used for model training and analysis is available at <https://github.com/learningmattermit/GLAMOUR>, and archived in Zenodo repository (Mohapatra, 2021).

ACKNOWLEDGEMENTS

SM acknowledges funding from Novo Nordisk and MIT’s Jameel Clinic, JA acknowledges funding from MIT’s UROP office. The authors thank Dr Daria Kim and Sarah Antilla from the Department of Chemistry, MIT for valuable comments.

REFERENCES

- Zeina Abu-Aisheh, Romain Raveaux, Jean-Yves Ramel, and Patrick Martineau. An Exact Graph Edit Distance Algorithm for Solving Pattern Recognition Problems. *4th International Conference on Pattern Recognition Applications and Methods*, 2015.
- Ethan C Alley, Grigory Khimulya, Surojit Biswas, Mohammed AlQuraishi, and George M Church. Unified rational protein engineering with sequence-based deep representation learning. *Nature methods*, 16(12):1315–1322, 2019.
- Stephen F Altschul, Warren Gish, Webb Miller, Eugene W Myers, and David J Lipman. Basic local alignment search tool. *Journal of molecular biology*, 215(3):403–410, 1990.
- Stephen F Altschul, Thomas L Madden, Alejandro A Schäffer, Jinghui Zhang, Zheng Zhang, Webb Miller, and David J Lipman. Gapped blast and psi-blast: a new generation of protein database search programs. *Nucleic acids research*, 25(17):3389–3402, 1997.
- Kiyoko F Aoki, Atsuko Yamaguchi, Yasushi Okuno, Tatsuya Akutsu, Nobuhisa Ueda, Minoru Kanehisa, and Hiroshi Mamitsuka. Efficient tree-matching methods for accurate carbohydrate database queries. *Genome informatics*, 14:134–143, 2003.
- H M Berman. The Protein Data Bank. *Nucleic Acids Research*, 28(1):235–242, jan 2000. ISSN 13624962. doi: 10.1093/nar/28.1.235. URL <http://www.ncbi.nlm.nih.gov/pubmed/10592235><http://www.pubmedcentral.nih.gov/articlerender.fcgi?artid=PMC102472><https://academic.oup.com/nar/article-lookup/doi/10.1093/nar/28.1.235>.
- Maxwell L. Bileschi, David Belanger, Drew Bryant, Theo Sanderson, Brandon Carter, D. Sculley, Mark A. DePristo, and Lucy J. Colwell. Using Deep Learning to Annotate the Protein Universe. *bioRxiv:10.1101/626507*, 2019.
- David B Blumenthal and Johann Gamper. On the exact computation of the graph edit distance. *Pattern Recognition Letters*, 134:46–57, 2020.
- Daniel Bojar, Rani K. Powers, Diogo M. Camacho, and James J. Collins. Deep-Learning Resources for Studying Glycan-Mediated Host-Microbe Interactions. *Cell Host and Microbe*, 29(1):132–144.e3, 2021.
- Grzegorz M Boratyn, Jean Thierry-Mieg, Danielle Thierry-Mieg, Ben Busby, and Thomas L Madden. Magic-blast, an accurate rna-seq aligner for long and short reads. *BMC bioinformatics*, 20(1):1–19, 2019.
- Karsten Borgwardt, Elisabetta Ghisu, Felipe Llinares-lópez, Leslie O Bray, and Bastian Rieck. Graph Kernels. *arXiv:2011.03854v2*, 2020.
- Rebekka Burkholz, John Quackenbush, and Daniel Bojar. Using graph convolutional neural networks to learn a representation for glycans. *Cell Reports*, 35(11):109251, 2021.
- Lihua Chen, Ghanshyam Pilania, Rohit Batra, Tran Doan Huan, Chiho Kim, Christopher Kuenneth, and Rampi Ramprasad. Polymer informatics: Current status and critical next steps. *Materials Science and Engineering: R: Reports*, 144:100595, 2021.
- Scott Clark and Patrick Hayes. SigOpt Web page. <https://sigopt.com>, 2019. URL <https://sigopt.com>.
- Lachlan Coff, Jeffrey Chan, Paul A Ramsland, and Andrew J Guy. Identifying glycan motifs using a novel subtree mining approach. *BMC bioinformatics*, 21(1):42, 2020.
- Axel Drefahl. Curlysmiles: a chemical language to customize and annotate encodings of molecular and nanodevice structures. *Journal of cheminformatics*, 3(1):1–7, 2011.
- Sean R Eddy. Where did the BLOSUM62 alignment score matrix come from? *Nature biotechnology*, 22(8):1035, 2004.

- Justin Gilmer, Samuel S. Schoenholz, Patrick F. Riley, Oriol Vinyals, and George E. Dahl. Neural Message Passing for Quantum Chemistry. *arXiv:1704.01212v2*, 2017.
- Aric A Hagberg, Daniel A Schult, and Pieter J Swart. Exploring Network Structure, Dynamics, and Function using NetworkX. In Gaël Varoquaux, Travis Vaught, and Jarrod Millman (eds.), *Proceedings of the 7th Python in Science Conference*, pp. 11–15, Pasadena, CA USA, 2008.
- William L Hamilton, Rex Ying, and Jure Leskovec. Representation learning on graphs: Methods and applications. *arXiv preprint arXiv:1709.05584*, 2017.
- Stephen R Heller, Alan McNaught, Igor Pletnev, Stephen Stein, and Dmitrii Tchekhovskoi. Inchi, the iupac international chemical identifier. *Journal of cheminformatics*, 7(1):1–34, 2015.
- Masae Hosoda, Yukie Akune, and Kiyoko F. Aoki-Kinoshita. Development and application of an algorithm to compute weighted multiple glycan alignments. *Bioinformatics*, 33(9):1317–1323, 2017.
- Tommi Jaakkola, Mark Diekhans, and David Haussler. A discriminative framework for detecting remote protein homologies. *Journal of Computational Biology*, 7(1-2):95–114, 2000.
- Wengong Jin, Regina Barzilay, and Tommi Jaakkola. Hierarchical generation of molecular graphs using structural motifs. In *International Conference on Machine Learning*, pp. 4839–4848. PMLR, 2020.
- Steven Kearnes, Kevin McCloskey, Marc Berndl, Vijay Pande, and Patrick F. Riley. Molecular graph convolutions: moving beyond fingerprints. *Journal of Computer-Aided Molecular Design*, 30(8): 595–608, 2016.
- Chiho Kim, Anand Chandrasekaran, Tran Doan Huan, Deya Das, and Rampi Ramprasad. Polymer Genome: A Data-Powered Polymer Informatics Platform for Property Predictions. *Journal of Physical Chemistry C*, 122(31):17575–17585, 2018.
- Sunghwan Kim, Jie Chen, Tiejun Cheng, Asta Gindulyte, Jia He, Siqian He, Qingliang Li, Benjamin A Shoemaker, Paul A Thiessen, Bo Yu, et al. Pubchem 2019 update: improved access to chemical data. *Nucleic acids research*, 47(D1):D1102–D1109, 2019.
- Thomas N. Kipf and Max Welling. Semi-supervised classification with graph convolutional networks. *5th International Conference on Learning Representations, ICLR 2017 - Conference Track Proceedings*, 2019.
- NM Kriege, FD Johansson, and C Morris. A survey on graph kernels. *appl netw sci* 5 (1): 6, 2020.
- Greg Landrum. RDKit: Open-source cheminformatics, 2006.
- Chee-Kong Lee, Chengqiang Lu, Yue Yu, Qiming Sun, Chang-Yu Hsieh, Shengyu Zhang, Qi Liu, and Liang Shi. Transfer learning with graph neural networks for optoelectronic properties of conjugated oligomers. *The Journal of Chemical Physics*, 154(2):024906, 2021.
- Christina Leslie, Eleazar Eskin, and William Stafford Noble. The spectrum kernel: A string kernel for svm protein classification. In *Biocomputing 2002*, pp. 564–575. World Scientific, 2001.
- Limin Li, Wai Ki Ching, Takako Yamaguchi, and Kiyoko F. Aoki-Kinoshita. A weighted q-gram method for glycan structure classification. *BMC Bioinformatics*, 11:1–6, 2010.
- Tzzy-Shyang Lin, Connor W Coley, Hidenobu Mochigase, Haley K Beech, Wencong Wang, Zi Wang, Eliot Woods, Stephen L Craig, Jeremiah A Johnson, and Julia A Kalow. BigSMILES: a structurally-based line notation for describing macromolecules. *ACS central science*, 5(9):1523–1531, 2019.
- Kevin McCloskey, Ankur Taly, Federico Monti, Michael P. Brenner, and Lucy J. Colwell. Using attribution to decode binding mechanism in neural network models for chemistry. *Proceedings of the National Academy of Sciences of the United States of America*, 116(24):11624–11629, 2019. ISSN 10916490. doi: 10.1073/pnas.1820657116.

- Leland McInnes, John Healy, and Steve Astels. hdbscan: Hierarchical density based clustering. *Journal of Open Source Software*, 2(11):205, 2017.
- Leland McInnes, John Healy, Nathaniel Saul, and Lukas Großberger. UMAP: Uniform Manifold Approximation and Projection. *Journal of Open Source Software*, 3(29):861, 2018.
- Somesh Mohapatra. learningmatter-mit/glamour: v0.1, August 2021. URL <https://doi.org/10.5281/zenodo.5237237>.
- Saul B. Needleman and Christian D. Wunsch. A general method applicable to the search for similarities in the amino acid sequence of two proteins. *Journal of Molecular Biology*, 48(3):443–453, 1970.
- Marion Neumann, Roman Garnett, Christian Bauckhage, and Kristian Kersting. Propagation kernels: efficient graph kernels from propagated information. *Machine Learning*, 102(2):209–245, 2016.
- Fabian Pedregosa, Gaël Varoquaux, Alexandre Gramfort, Vincent Michel, Bertrand Thirion, Olivier Grisel, Mathieu Blondel, Peter Prettenhofer, Ron Weiss, Vincent Dubourg, et al. Scikit-learn: Machine learning in python. *the Journal of machine Learning research*, 12:2825–2830, 2011.
- Malak Pirtskhalava, Andrei Gabrielian, Phillip Cruz, Hannah L Griggs, R Burke Squires, Darrell E Hurt, Maia Grigolava, Mindia Chubinidze, George Gogoladze, Boris Vishnepolsky, et al. Dbaasp v. 2: an enhanced database of structure and antimicrobial/cytotoxic activity of natural and synthetic peptides. *Nucleic acids research*, 44(D1):D1104–D1112, 2016.
- Ana Planinc, Jonathan Bones, Bieke Dejaeger, Pierre Van Antwerpen, and Cédric Delporte. Glycan characterization of biopharmaceuticals: updates and perspectives. *Analytica chimica acta*, 921: 13–27, 2016.
- Bo Qiao, Somesh Mohapatra, Jeffrey Lopez, Graham M. Leverick, Ryoichi Tatara, Yoshiki Shibuya, Yivan Jiang, Arthur France-Lanord, Jeffrey C. Grossman, Rafael Gómez-Bombarelli, Jeremiah A. Johnson, and Yang Shao-Horn. Quantitative Mapping of Molecular Substituents to Macroscopic Properties Enables Predictive Design of Oligoethylene Glycol-Based Lithium Electrolytes. *ACS Central Science*, 6(7):1115–1128, 2020.
- Kaspar Riesen and Horst Bunke. Approximate graph edit distance computation by means of bipartite graph matching. *Image and Vision Computing*, 27(7):950–959, 2009.
- David Rogers and Mathew Hahn. Extended-Connectivity Fingerprints. *J. Chem. Inf. Model.*, 50(5): 742–754, 2010.
- Benjamin Sanchez-Lengeling, Jennifer N Wei, Brian K Lee, Richard C Gerkin, Alán Aspuru-Guzik, and Alexander B Wiltschko. Machine learning for scent: learning generalizable perceptual representations of small molecules. *arXiv preprint arXiv:1910.10685*, 2019.
- Benjamin Sanchez-Lengeling, Jennifer Wei, Brian Lee, Emily Reif, Peter Y Wang, Wei Qian, Kevin Mccloskey, Lucy Colwell, and Alexander Wiltschko. Evaluating Attribution for Graph Neural Networks. *Proceedings of the Neural Information Processing Systems Conference*, (NeurIPS), 2020.
- Carly K Schissel, Somesh Mohapatra, Justin M Wolfe, Colin M Fadzen, Kamela Bellovoda, Chia-Ling Wu, Jenna A Wood, Annika B Malmberg, Andrei Loas, Rafael Gómez-Bombarelli, et al. Deep learning to design nuclear-targeting abiotic miniproteins. *Nature Chemistry*, pp. 1–9, 2021.
- Kristof T. Schütt, P.-J J. Pieter-Jan P.-J Pieter-Jan Kindermans, Huziel E. Saucedo, Stefan Chmiela, Alexandre Tkatchenko, and Klaus-Robert R. Müller. SchNet: A continuous-filter convolutional neural network for modeling quantum interactions. *Advances in Neural Information Processing Systems*, 2017-Decem(1):992–1002, jun 2017. URL <http://arxiv.org/abs/1706.08566>www.quantum-machine.org.
- Seokjun Seo, Minsik Oh, Youngjune Park, and Sun Kim. Deepfam: deep learning based alignment-free method for protein family modeling and prediction. *Bioinformatics*, 34(13):i254–i262, 2018.

- Avanti Shrikumar, Peyton Greenside, and Anshul Kundaje. Learning important features through propagating activation differences. *arXiv:1704.02685*, 2017.
- Giannis Siglidis, Giannis Nikolentzos, Stratis Limnios, Christos Giatsidis, and Michalis Vazirgianis. GraKeL : A Graph Kernel Library in Python. *Journal of Machine Learning Research*, 21: 1–5, 2020.
- Temple F Smith and Michael S Waterman. Identification of common molecular subsequences. *Journal of molecular biology*, 147(1):195–197, 1981.
- Peter C. St John, Caleb Phillips, Travis W. Kemper, A. Nolan Wilson, Yanfei Guan, Michael F. Crowley, Mark R. Nimlos, and Ross E. Larsen. Message-passing neural networks for high-throughput polymer screening. *Journal of Chemical Physics*, 150(23), 2019.
- Mahito Sugiyama, M. Elisabetta Ghisu, Felipe Llinares-López, and Karsten Borgwardt. Graphkernels: R and Python packages for graph comparison. *Bioinformatics*, 34(3):530–532, 2018.
- Mukund Sundararajan, Ankur Taly, and Qiqi Yan. Axiomatic attribution for deep networks. *arXiv:1703.01365*, 2017.
- Laurens Van Der Maaten and Geoffrey Hinton. Visualizing Data using t-SNE. *Journal of Machine Learning Research*, 9:2579–2605, 2008.
- Petar Velickovic, Guillem Cucurull, Arantxa Casanova, Adriana Romero, Pietro Lio, and Yoshua Bengio. Graph Attention Networks. *arXiv:1710.10903*, 2017.
- Minjie Wang, Da Zheng, Zihao Ye, Quan Gan, Mufei Li, Xiang Song, Jinjing Zhou, Chao Ma, Lingfan Yu, Yu Gai, Tianjun Xiao, Tong He, George Karypis, Jinyang Li, and Zheng Zhang. Deep Graph Library: A Graph-Centric, Highly-Performant Package for Graph Neural Networks. *arXiv:1909.01315*, 2019.
- Zhaoping Xiong, Dingyan Wang, Xiaohong Liu, Feisheng Zhong, Xiaozhe Wan, Xutong Li, Zhaojun Li, Xiaomin Luo, Kaixian Chen, Hualiang Jiang, and Mingyue Zheng. Pushing the boundaries of molecular representation for drug discovery with the graph attention mechanism. *Journal of Medicinal Chemistry*, 63(16):8749–8760, 2020.
- Yoshihiro Yamanishi, Francis Bach, and Jean-Philippe Vert. Glycan classification with tree kernels. *Bioinformatics*, 23(10):1211–1216, 2007.
- Kevin Yang, Kyle Swanson, Wengong Jin, Connor Coley, Philipp Eiden, Hua Gao, Angel Guzman-Perez, Timothy Hopper, Brian Kelley, Miriam Mathea, et al. Analyzing learned molecular representations for property prediction. *Journal of chemical information and modeling*, 59(8):3370–3388, 2019.
- Minggang Zeng, Jatin Nitin Kumar, Zeng Zeng, Ramasamy Savitha, Vijay Ramaseshan Chandrasekhar, Kedar Hippalgaonkar, and Electronic Materials. Graph Convolutional Neural Networks for Polymers. *arXiv:1811.06231v1*, 2018.
- Tianhong Zhang, Hongli Li, Hualin Xi, Robert V Stanton, and Sergio H Rotstein. Helm: a hierarchical notation language for complex biomolecule structure representation, 2012.
- Zhenjie Zhang, Marios Hadjieleftheriou, Beng Chin Ooi, and Divesh Srivastava. Bed-tree: an all-purpose index structure for string similarity search based on edit distance. In *Proceedings of the 2010 ACM SIGMOD International Conference on Management of data*, pp. 915–926, 2010.
- Jie Zhou, Ganqu Cui, Zhengyan Zhang, Cheng Yang, Zhiyuan Liu, Lifeng Wang, Changcheng Li, and Maosong Sun. Graph Neural Networks: A Review of Methods and Applications. *arXiv:1812.08434v4*, 2018.

APPENDIX

A RELATED WORK

Representation. Macromolecules can be represented as strings, using hierarchical editing language for macromolecules (HELM) (Zhang et al., 2012), International Union of Pure and Applied Chemistry (IUPAC) international chemical identifier (InChI) (Heller et al., 2015), CurlySMILES (Drefahl, 2011) (where SMILES is Simplified Molecular-Input Line-Entry System) and BigSMILES (Lin et al., 2019). Line notations do not always support all topologies, require a fair amount of customization, and have non-canonical variants. One exception to this is linear biological macromolecules, such as proteins and DNA/RNA, which are represented as sequences of one/three-letter monomer codes. In a recent attempt, glycans (non-linear biological macromolecules) were represented as sequences, where groups of monosaccharides were clubbed into 'glycowords' and placed in hierarchical brackets (Bojar et al., 2021). Representing glycans presents a significant advance in notation but falls short in terms of comparison (limited to linear glycans) and machine learning tasks.

Hierarchical fingerprinting is another approach, which follows a hierarchy of atomic (categorical encoding of presence/absence of contiguous atom-sets), physicochemical (e.g., fraction of rings, molecular surface area), and morphological descriptors (e.g., length of side chain, length of main chain) (Kim et al., 2018). This approach is limited in its coverage of chemical space, ability to differentiate stereochemistry, and capturing long range through-space interactions.

Similarity computation. In recent times, there have been significant advances in computation of similarity using graph edit distances (Blumenthal & Gamper, 2020) (GED) and graph kernels (Borgwardt et al., 2020; Kriege et al., 2020). Development of software packages, such as graphkernels (Sugiyama et al., 2018) and GraKeL (Siglidis et al., 2020), has provided fast implementations of graph kernels.

For linear biological macromolecules, such as proteins, DNA/RNA and linear glycans, there are several works for computation of sequence similarities (Bojar et al., 2021; Altschul et al., 1990; 1997; Boratyn et al., 2019). Usually, sequence alignment is done using Smith-Waterman (Smith & Waterman, 1981) or Needleman-Wunsch (Needleman & Wunsch, 1970) algorithms, and scored with substitution matrices, such as BLOSUM62 (Eddy, 2004) (for proteins) and GLYSUM (Bojar et al., 2021) (for glycans). These substitution matrices are based on evolutionary statistics thereby biasing the scoring towards the statistical frequency of a particular monomer's occurrence in the course of evolution, rather than chemical similarity. Apart from sequence alignment in linear macromolecules, edit distances (Riesen & Bunke, 2009; Zhang et al., 2010), linear kernels (Leslie et al., 2001; Jaakkola et al., 2000) and deep learning methods (Bileschi et al., 2019; Seo et al., 2018) have been proposed to compute similarity. In the case of non-linear macromolecules, alignment of glycans has been explored using q-grams (Li et al., 2010), tree matching methods (Aoki et al., 2003; Hosoda et al., 2017; Coff et al., 2020), and using tree kernels (Yamanishi et al., 2007). Unfortunately, the aforementioned methods are limited to biological macromolecules, and do not extend to the general macromolecular chemical space. Moreover, existing tools do not allow incorporation of unnatural monomers and non-linear topologies (except glycans).

Machine learning. The field of graph neural networks (GNN) has seen substantial developments in both model architecture and attribution. The different model architectures have demonstrated state-of-the-art results across various domains - graph convolutional network (GCN), graph attention network (GAT), message passing neural network (MPNN), SchNet, Weave (a variant of GCN), and AttentiveFP (a variant of GAT) (Zhou et al., 2018; Schütt et al., 2017; Kearnes et al., 2016; Xiong et al., 2020). Graph attribution has been recently studied quantitatively across four metrics - accuracy, stability, faithfulness and consistency - for a wide variety of tasks and model architectures (Sanchez-Lengeling et al., 2020).

For macromolecular property prediction, Polymer Genome and similar works using hierarchical fingerprints predict glass transition temperature, dielectric point and other macromolecular properties (Kim et al., 2018; Chen et al., 2021). There have been several attempts to extrapolate macromolecular property by training over monomer input features (St John et al., 2019; Qiao et al., 2020; Lee et al., 2021). GCN over macromolecule graphs with one-hot node and edge attributes has been shown to outperform fingerprint-based models (Zeng et al., 2018). For fingerprint-based models,

the lack of a good macromolecule representation limits the model performance, while the GCN model is limited by the lack of chemical information in the graph representation.

B DATASET PROCESSING

B.1 GLYCANS

B.1.1 DATASET DOWNLOAD

A dataset of 19299 glycans was accessed and downloaded from GlycoBase (accessed on November 2, 2020) (Bojar et al., 2021). The file contained GlycoBase ID, sequence, link (N, O, free, or none), species, and immunogenicity information for each glycan.

For each glycan sequence string the brackets denote branches, with the point of attachment/bonding of the branch as the monomer immediately after the brackets. The first element within the bracket is the monomer most distant from the point of attachment, and the last element within the bracket is the abbreviation of the bond that connects the branch to the original main chain. Nested brackets indicate additional sub-branches off of branches, and multiple sets of brackets next to each other indicate several branches off of the same monomer.

B.1.2 DATASET PRE-PROCESSING

7 modifications and 152 deletions of glycan sequences were made before the process for situations such as an unequal number of opening and closing brackets and dangling branches without specified connectivity. Additional glycan sequences were removed due to missing SMILES sequences for a number of monomers. The original GlycoBase.csv file was curated to reflect the modification and deletion changes, resulting in a total of 19147 glycans.

Using the curated database, we visualized the distribution of species of origin, link, and immunogenicity of the glycans (Figures A.1, A.2, A.3).

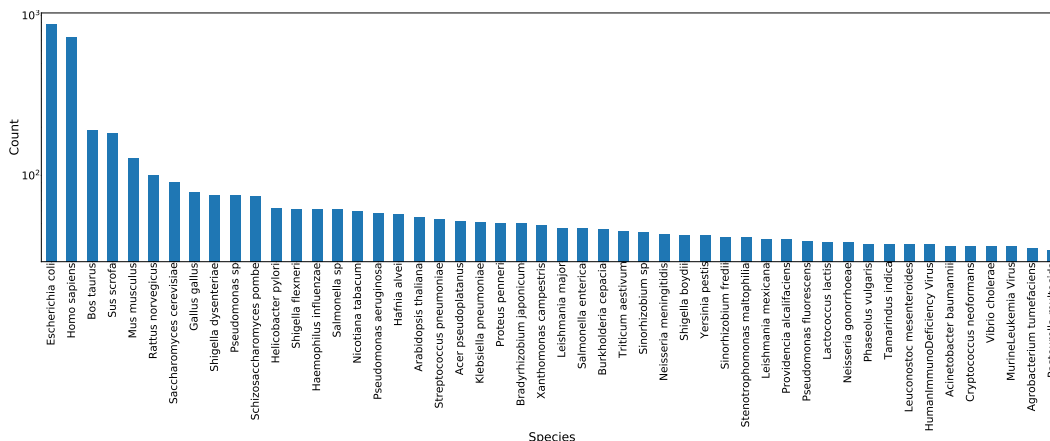


Figure A.1: Top 50 most common glycan species of origin, sorted in descending order of count with y-axis on a logarithmic scale.

B.1.3 SMILES COMPILATION

The chemical composition and formula of the 959 monomers (also known as glycoletters in GlycoBase) and 53 bonds were expressed as isomeric simplified molecular-input line-entry system (SMILES) sequences.

In the dataset retrieved from GlycoBase, all position-specific information about monomer modifications was removed. The supplementary information of SweetTalk contains all the raw glycan sequences before position-specific modification information was removed (Bojar et al., 2021). While

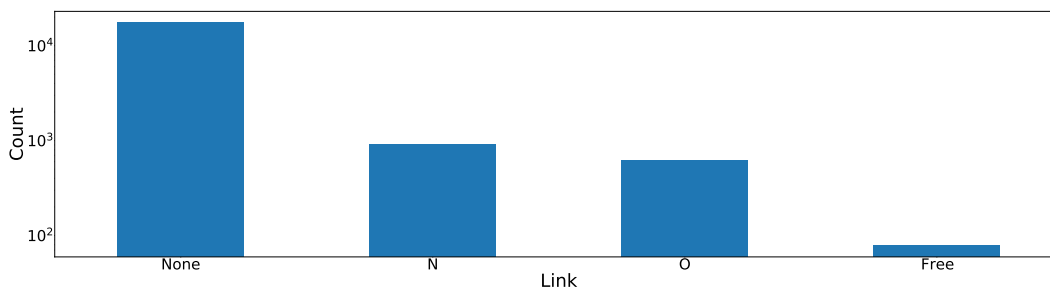


Figure A.2: Four types of glycan links sorted in descending order of count with y-axis on a logarithmic scale.

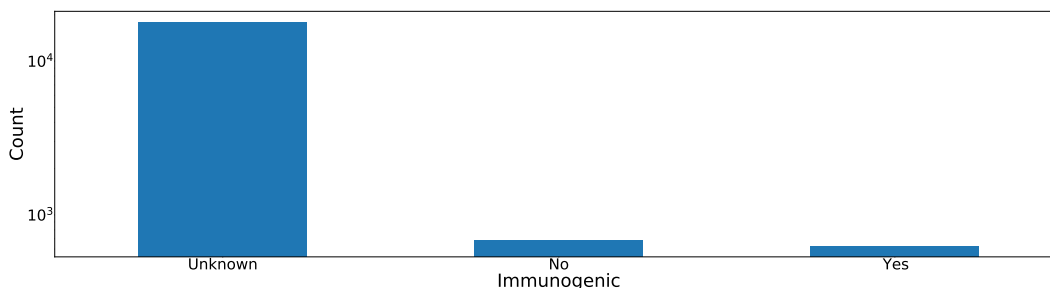


Figure A.3: Three different types of glycan immunogenicity labels sorted in descending order of count, with y-axis on a logarithmic scale.

insufficient information is provided to directly match the raw sequences with the corresponding edited sequences, the raw sequences can be used to look for trends and most common modification positions for each monomer. A dictionary was created to describe the number of times each monomer appears in all the raw sequences. A couple of terms should be defined for consistency:

- “Monosaccharides” refer to the individual glycoletters without any modifications, such as D-glucose (D-Glu) and galactose (D-Gal). The term “monosaccharide” is simplistic because it also covers alcohols, acids, and other classes of molecules, but the term will be employed for the sake of consistency and clarity.
- “Modifications” refer to substitutions or additions to the original monosaccharide sequence such as a nitrogen-linked acetyl group (NAc) and oxygen-linked methyl group (OMe). In this dataset, monosaccharides can have between 0-4 modifications.
- “Monomers” refer to the combination of the monosaccharide and modification(s), also known as glycoletters in GlycoBase.

Using the raw monomers dictionary, the positions of the modifications for each monomer in the corresponding SMILES were set using a list of consistent rules outlined below. The rules are listed in order of priority.

1. For each monomer/glycoletter, if at least one monomer with the same monosaccharide and set of modifications exists in the raw monomers dictionary, assume the set of positions with the highest frequency. If no monomer exists in the raw monomers dictionary with the same monosaccharide and set of modifications, proceed to the following steps.
2. If the monomer has a hydroxyl group at the 2 position, is not a furanose or ketose, and contains a nitrogen-linked modification (N, NBut, NMe, etc.), assign the first occurrence of a nitrogen-linked modification to the 2 position.
3. If the monomer is a hexose or deoxy-hexose and contains a pyruvate acetal (OPyr), assume that the acetal connects the 4 and 6 positions.

4. If the monomer contains an O-linked phosphate (OP) or sulfate (OS) modification, search the raw monomers dictionary for instances of the monosaccharide with only the OP/OS modification and assume the most frequent position.
5. If the monomer contains a variant of the O-linked phosphate modification (OPETn, OPPEtn, etc.), assign the OP-variant modification the same position as the most common position for the OP modification on the monosaccharide.
6. If the monomer contains two modifications, search the raw glycans dictionary for instances of the monosaccharide with only each modification separately but not at the same time. Assign each modification the position of highest frequency. If either monosaccharide and modification combination does not exist in the raw monomers dictionary and the monomer is a hexose, assign positions in the following order: 2, 4, 3, 6. If the position is already occupied from previous steps or does not exist in a deoxy hexose, skip to the position with next highest priority.
7. If the monomer is a hexose or deoxy-hexose and contains more than two modifications, assign positions in the following order: 2, 3, 4, 6. If the position is already occupied from previous steps or does not exist in a deoxy hexose, skip to the position with next highest priority.
8. Assume all amino acids are connected to the monosaccharide via the oxygen on the carboxyl. If the connectivity is not specified for a group following the amino acid (CysAc, AlaFo), assume that the group following the amino acid is connected to the amino acid via the amine group.
9. For neuraminic acid (Neu), ketodeoxynononic acid (Kdn), pseudaminic acid (Pse), legionaminic acid (Leg), and other similar ketose-based acids, assign modification positions in the following order: 1, 4.
10. For fructofuranose and similar furanoses for which the 1-position is not part of the ring, assign modifications in the following order: 1, 3, 4.
11. For alcohols, follow the same rules that apply to the oxidized form of the alcohol. For example, for glucitol follow the same rules that apply to glucose.
12. Assume all rare monosaccharides (denoted as Sug) are hexoses with no specified stereochemistry.

Because the 959 monomers contained some repeat SMILES sequences with different monomer names, 13 redundant names were deleted so that each distinct monomer SMILES only appears once in the SMILES compilation.

The SMILES for the 53 bond types differ in stereochemistry alone (alpha, beta, or unspecified) but all have the same chemical composition of a glycosidic bond. Each bond is expressed as a variation of the SMILES sequence CC(OC)CC, which consists of the glycosidic bond C-O-C with one of the C atoms also connected to both a methyl and ethyl group. The chiral C with the four different attached groups is used to specify the alpha or beta stereochemistry displayed in the bond name. The stereochemistry at the tetrahedral C is consistently S for all alpha bonds, R for all beta bonds, and not specified for all unspecified bonds. The 53 bond names were condensed into 3 distinct bond types differing in stereochemistry alone.

B.2 ANTI-MICROBIAL PEPTIDES

B.2.1 DATASET DOWNLOAD

A dataset of 15864 antimicrobial peptides (AMPs), including 15450 monomers, 200 multimers, and 214 multi-peptides, from the Database of Antimicrobial Activity and Structure of Peptides (DBAASP) was accessed and downloaded on October 6, 2020 (Pirtskhalava et al., 2016).

Each peptide was represented in the dataset as an individual .json file containing information about the peptide ID, name, sequence(s), unusual amino acids, connectivity, terminal modifications, complexity, synthesis type, target groups and objects, and target species. The term “target species” is used loosely and actually encompasses both species and sub-classification information such as sub-species, strain for bacteria, and forma speciales for fungi. For each target species for any given

peptide, the dataset provides the antimicrobial peptide concentration in units of mostly either μM or $\mu\text{g/mL}$ as a function of four unique variables: activity measure, salt type, medium, and CFU.

The dataset includes three different types of peptide complexities: monomers, multimers, and multi-peptides. In the DBAASP dataset, monomers consist of a single sequence, multimers between 2 and 4 separate sequences connected via interchain bonds, and multi-peptides between 2 and 4 separate sequences connected not via covalent bonds but instead weaker intermolecular forces.

B.2.2 DATASET PRE-PROCESSING

The information from each .json file was inputted into a combined table and the antimicrobial peptide concentrations for each target species was converted into a float value by removing symbols like '>' and '<', taking the average whenever the dataset provides a range, and disregarding uncertainty values.

9 peptide monomer types included in a total of 86 peptides were removed due to ambiguity of the molecular structure, bringing the total number of peptides to 15,778. This condensed dataset was further processed to visualize the distribution of target species data points. For each “target species,” the species name was separated from any sub-classifications (subspecies, strain, forma specialis, serovar, pathovar, biovar, etc.).

Using the processed database, we visualized the distribution of species, activity measure, salt types, mediums, units, and CFU in the target species data points (Figures A.4-A.9).

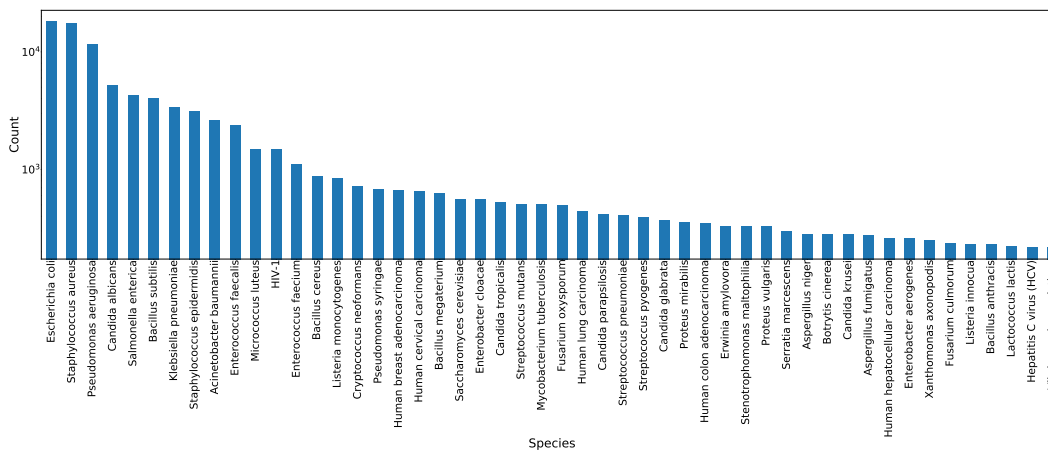


Figure A.4: Top 50 species with greatest number of data points sorted in descending order of count, with y-axis on a logarithmic scale.

As evident from the bar plots, the vast majority of data points belong to either *Escherichia coli* or *Staphylococcus aureus*. To understand whether the overall dataset could be further filtered to limit the variability in conditions for more meaningful comparison of peptide concentrations, we visualized the distribution of activity measure and salt type for both *E. coli* (Figures A.10, A.11) and *S. aureus* (Figures A.12, A.13).

For both *E. coli* and *S. aureus*, the majority of data points have an activity measure of MIC and no added salt. Due to the clear majority for both activity measure and salt type as well as the difficulty of interconversion between the units of μM and $\mu\text{g/mL}$, the overall dataset was filtered into two separate, smaller datasets: one containing only data points falling into all of the categories of *E. coli*, MIC, no salt, and μM data points and the other containing only data points falling into all of the categories of *S. aureus*, MIC, no salt, and μM . Each of the two sub-datasets was further filtered to remove any peptides for which the standard deviation of the peptide concentrations meeting the criteria for the sub-dataset was not zero, resulting in a total of 4,445 peptides for the *E. coli* dataset and 3,686 peptides for the *S. aureus* dataset.

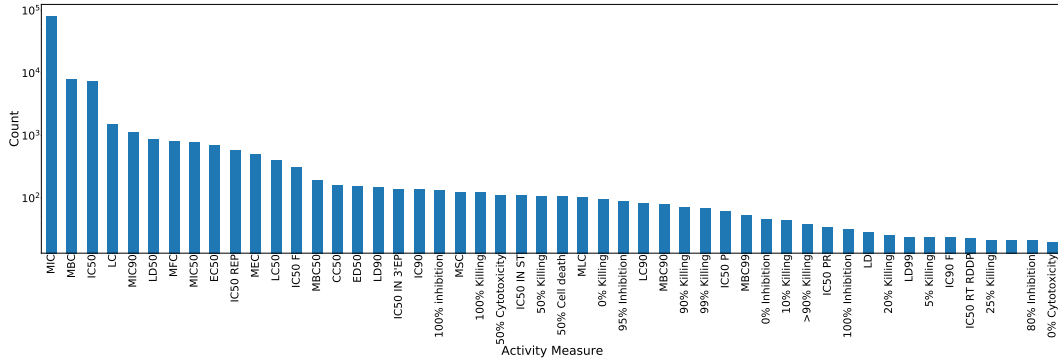


Figure A.5: Top 50 activity measures with greatest number of data points sorted in descending order of count, with y-axis on a logarithmic scale.

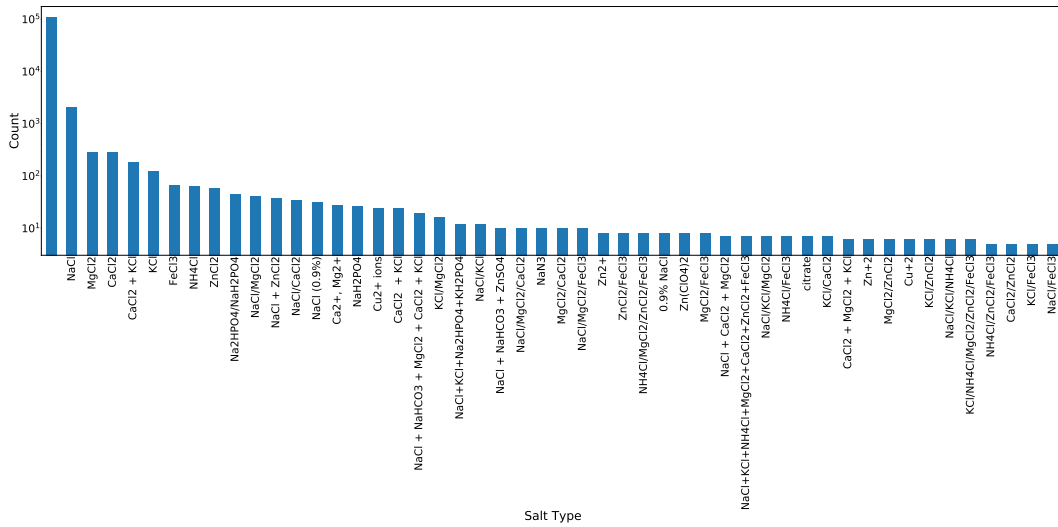


Figure A.6: Top 50 salt types with greatest number of data points sorted in descending order of count, with y-axis on a logarithmic scale. The blank label for the first column indicates the absence of any added salt.

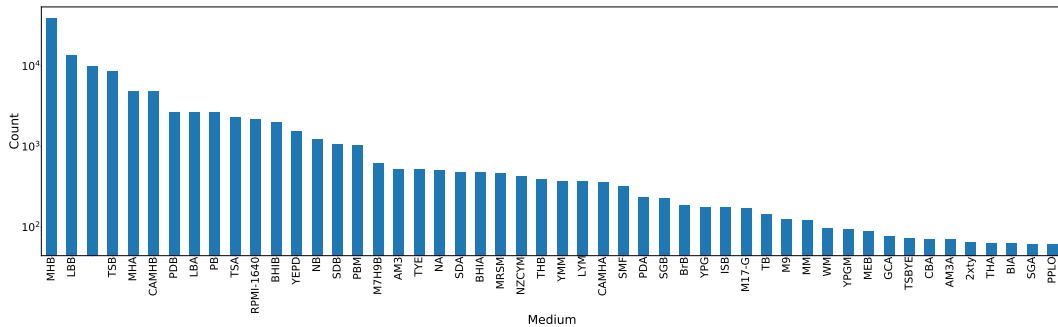


Figure A.7: Top 50 mediums with greatest number of data points sorted in descending order of count, with y-axis on a logarithmic scale.

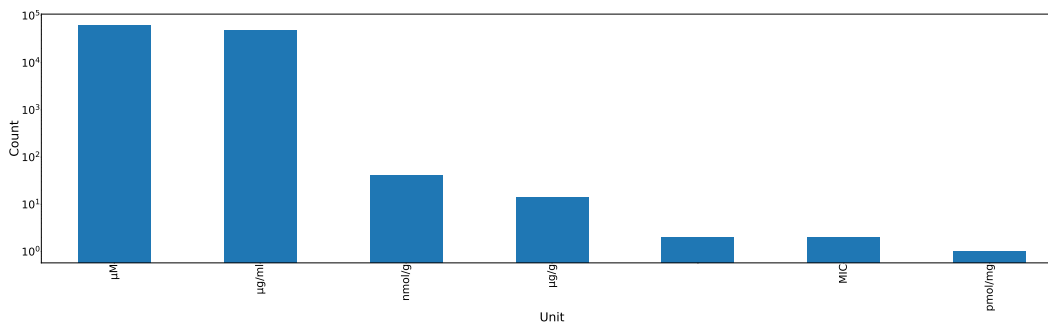


Figure A.8: All peptide concentration units sorted in descending order of count, with y-axis on a logarithmic scale.

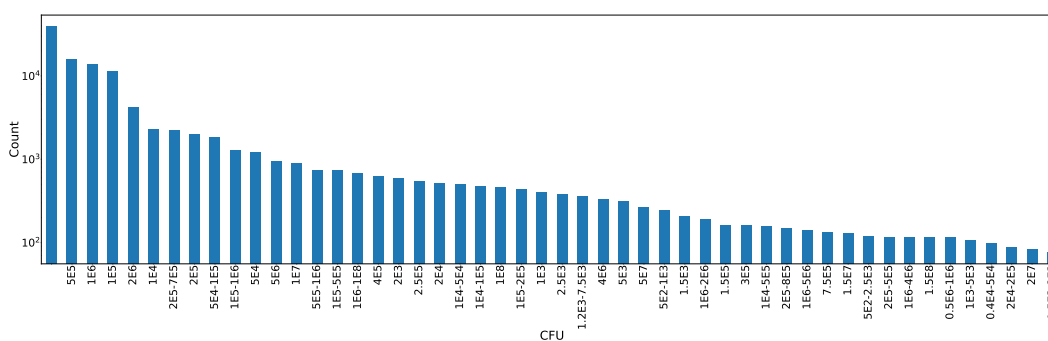


Figure A.9: Top 50 CFUs with greatest number of data points sorted in descending order of count, with y-axis on a logarithmic scale.

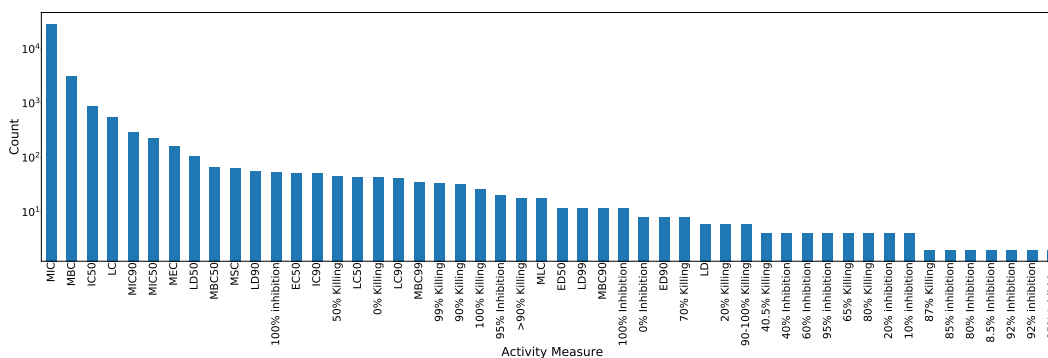


Figure A.10: Top 50 activity measures for *E. coli* data points with greatest number of occurrences sorted in descending order of count, with y-axis on a logarithmic scale.

B.2.3 SMILES COMPILATION

The chemical composition and formula of the 332 amino acids, 93 N-termini modifications, 37 C-termini modifications, and 22 bonds were expressed as isomeric simplified molecular-input line-entry system (SMILES) sequences. The majority of isomeric SMILES sequences were found on PubChem from the National Library of Medicine (Kim et al., 2019). The remaining SMILES were collected through review of literature cited in the DBAASP peptide cards of peptides containing the corresponding monomers or bonds.

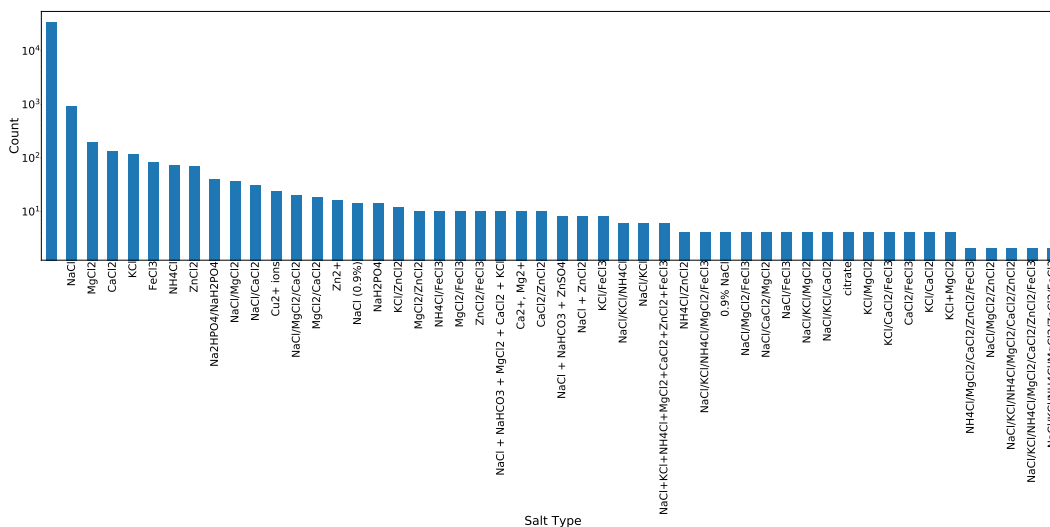


Figure A.11: Top 50 salt types for *E. coli* data points with greatest number of occurrences sorted in descending order of count, with y-axis on a logarithmic scale. The blank label for the first column indicates the absence of any added salt.

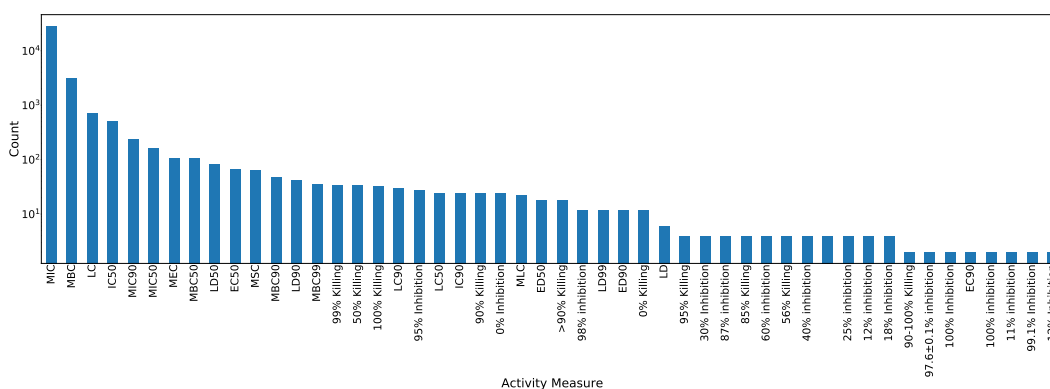


Figure A.12: Top 50 activity measures for *S. aureus* data points with greatest number of occurrences sorted in descending order of count, with y-axis on a logarithmic scale.

For the monomers, no additional sequences beyond those of the 20 standard L-amino acids and unusual amino acids, C-termini modifications, and N-termini modifications found in the Help section of the DBAASP website were included in the SMILES compilation. 8 monomers had repeat names between the three different types of monomers, and the names were changed so that each monomer corresponds with a unique name. For the bonds, the sidechain-mainchain bonds (SMB) were split into 7 subtypes determined through review of the literature. In addition, 6 additional bond types were added for cases in which the connection between the N or C-termini modification and terminal amino acid is not an amide bond. The 7 SMB subtypes, 6 additional terminal bond types, and 9 intrachain bond types in the Help section of the DBAASP website resulted in a total of 22 bonds.

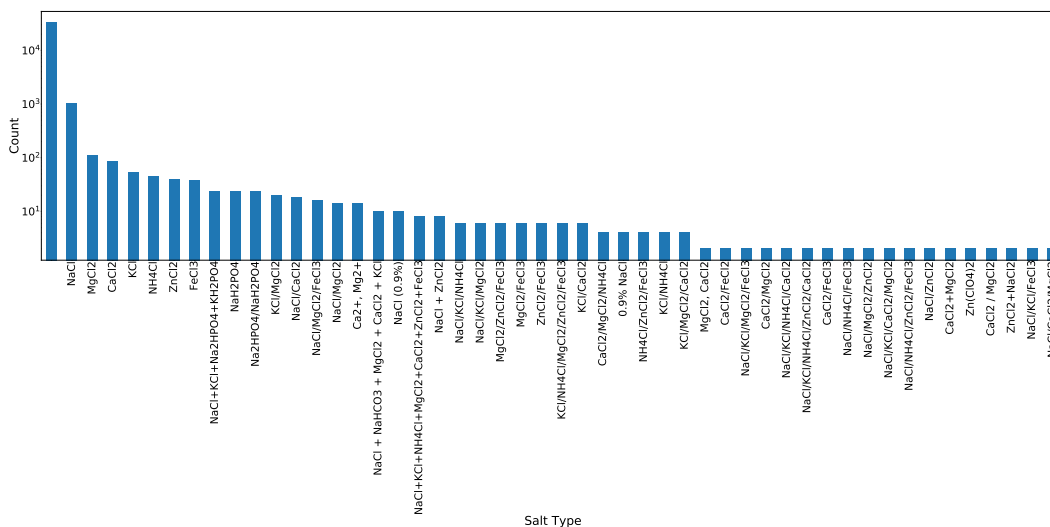


Figure A.13: Top 50 salt types for *S. aureus* data points with greatest number of occurrences sorted in descending order of count, with y-axis on a logarithmic scale. The blank label for the first column indicates the absence of any added salt.

C TEXT FILE SYSTEM

C.1 FORMAT

The text files to convert each macromolecule structure into machine-readable format consist of three sections: the SMILES sequences for each unique monomer or bond, the positions of each monomer, and the two monomer positions connected by each bond. Each section starts with a header to indicate the start of a new part. The first section contains the abbreviation of each unique monomer or bond in the glycan followed by the corresponding SMILES sequence, with each entry on a separate line. The monomers section consists of the monomer position followed by the monomer abbreviation. The bonds section contains the two connectivity positions in the glycan for the bond separated by a space, followed by the bond abbreviation (Figure A.14).

C.2 TEXT FILE PARSER

A text file parser converts the macromolecule information stored in the .txt file to a NetworkX graph with monomers expressed as nodes and bonds expressed as edges. The parser goes through the .txt file line by line, stores the monomer information in a dictionary with keys as integer positions and values as monomer abbreviations, and stores the bond information in a dictionary with keys as tuples containing bond connectivities and values as bond abbreviations. Afterwards, the reader uses NetworkX to add each key in the monomer dictionary as a node and each key in the bond dictionary as an edge, storing the abbreviations as attributes for the corresponding node or edge. The resulting NetworkX graphs include both linear and highly branched architectures (Figure A.15, A.16).

D NODE AND EDGE ATTRIBUTES

D.1 FINGERPRINTS – GENERATION AND OPTIMIZATION OF HYPERPARAMETERS

We used RDKit to generate stereochemical extended connectivity fingerprints (Landrum, 2006; Rogers & Hahn, 2010). Radius and number of bits were optimized by calculating mean and standard deviation, and visualizing the distribution of Tanimoto similarity of all monomers in the glycans dataset (Figure A.17A-C). We aimed to obtain fingerprints with lower number of bits and optimal radius that could represent the monomer aptly in both similarity computation and graph neural network models. For 64 bits, we observed that the mean similarity was as high as 0.4 and standard

SMILES of unique monomers and bonds	1	SMILES
	2	C C([C@@H](C(=O)O)N)S
	3	K C(CCN)C[C@@H](C(=O)O)N
	4	A C[C@@H](C(=O)O)N
	5	F C1=CC=C(C=C1)C[C@@H](C(=O)O)N
	6	DSB CSSC
	7	AMB CNC(C)=O
	8	
Monomer positions and abbreviations	9	MONOMERS
	10	1 C
	11	2 K
	12	3 A
	13	4 A
	14	5 F
	15	6 C
	16	
Bond connectivities and abbreviations	17	BONDS
	18	1 6 DSB
	19	1 2 AMB
	20	2 3 AMB
	21	3 4 AMB
	22	4 5 AMB
	23	5 6 AMB

Figure A.14: Standard text file format with three sections: SMILES of unique monomers and bonds, monomer positions and abbreviations, and bond connectivities and abbreviations.

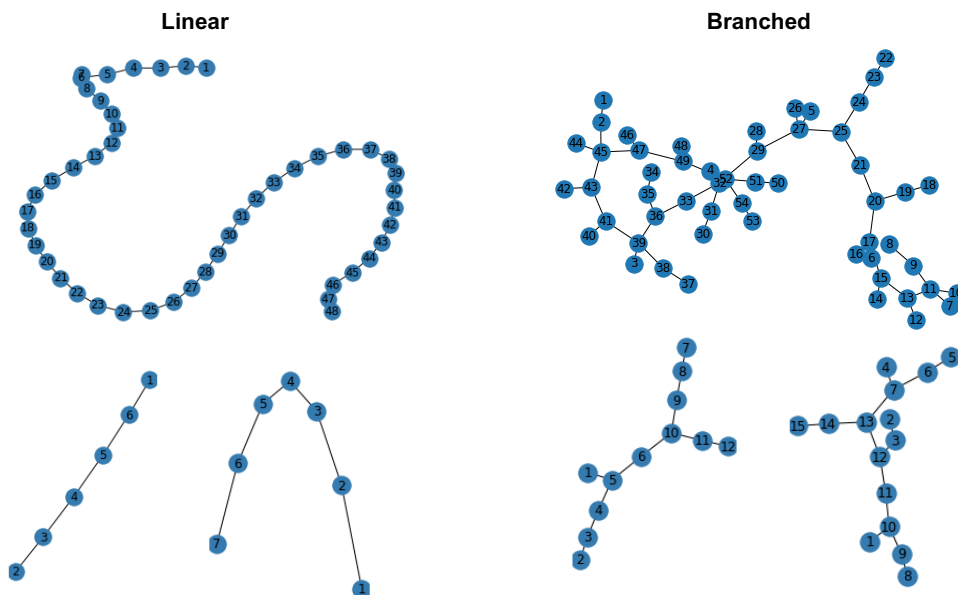


Figure A.15: NetworkX graph representations of glycans that consist of both linear and highly branched architectures of varying molecular weights and complexities.

deviation for similarity went up after radius 3 indicating higher hash collision and lesser differentiability. For 128 bits, the mean and standard deviation plateaued around 0.3 and 0.08, respectively. Further, the similarity distribution was qualitatively spread over a larger range, as compared to fingerprints with larger number of bits. For fingerprint bits longer than 128, we observed lower mean and standard deviation, and decreasing spread in the similarity distribution. The decreasing trend

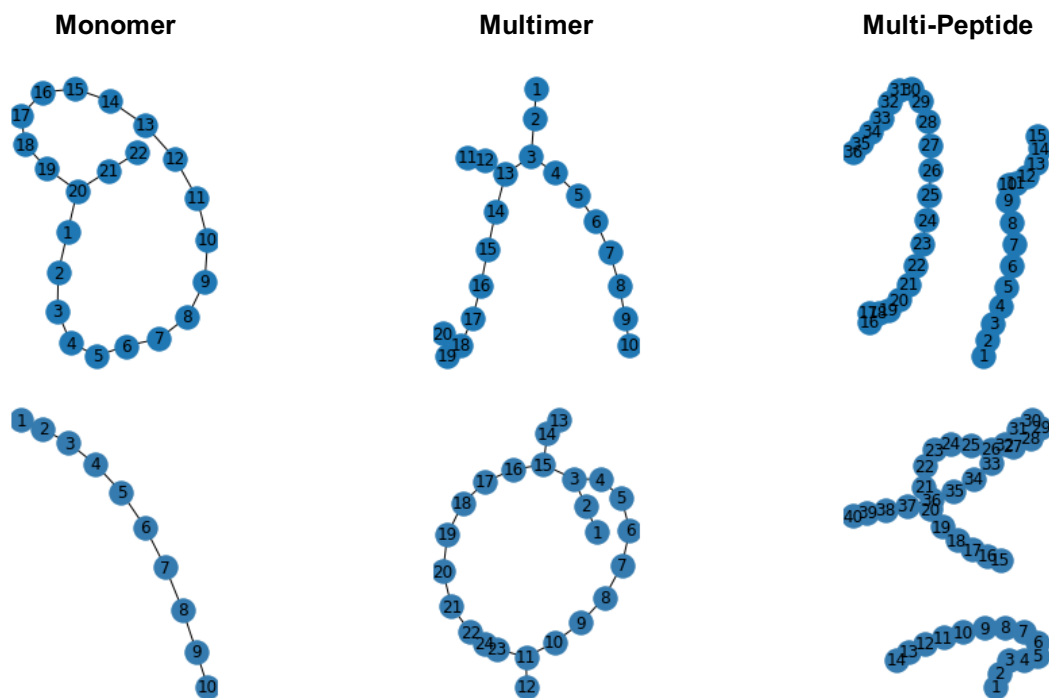


Figure A.16: NetworkX graph representations of peptides of all three complexities of varying molecular weights.

indicates that the fingerprints with bits higher than 128 are equally dissimilar, thus, if used, will lead to glycans with equally high dissimilar scores. Hence, we chose fingerprints with 128 bits and radius 3 to generate node attributes for glycans. For edge attributes, we had 3 types of glycosidic bonds differing by the stereochemistry alone, hence, we chose fingerprints with 16 bits and radius 3. We employed similar reasoning for the peptides to select 128 bits and radius 3 for both monomers and bonds.

We observed that there were 3 sets with 7 glycans which had exact fingerprints (Figure A.17D). Since, the difference was in the number of carbon atoms in the aliphatic chain, we used the fingerprints as is.

D.2 ONE-HOT ENCODING BENCHMARK

One-hot encodings of the 946 monomer and 3 bond types for glycans and the 461 monomer and 22 bond types for peptides were also employed as feature types for benchmarking with featurization using molecular fingerprints. The dimensions of the node and edge one-hot encoding features are 946 and 3, respectively, for glycans and 461 and 22, respectively, for peptides.

E SIMILARITY COMPUTATION

E.1 ANALYSIS OF GRAPHS

Most glycan graphs are sparse (Figure A.8). Complete graphs have density of 1, while graphs with density > 0.5 have been defined as dense (Borgwardt et al., 2020).

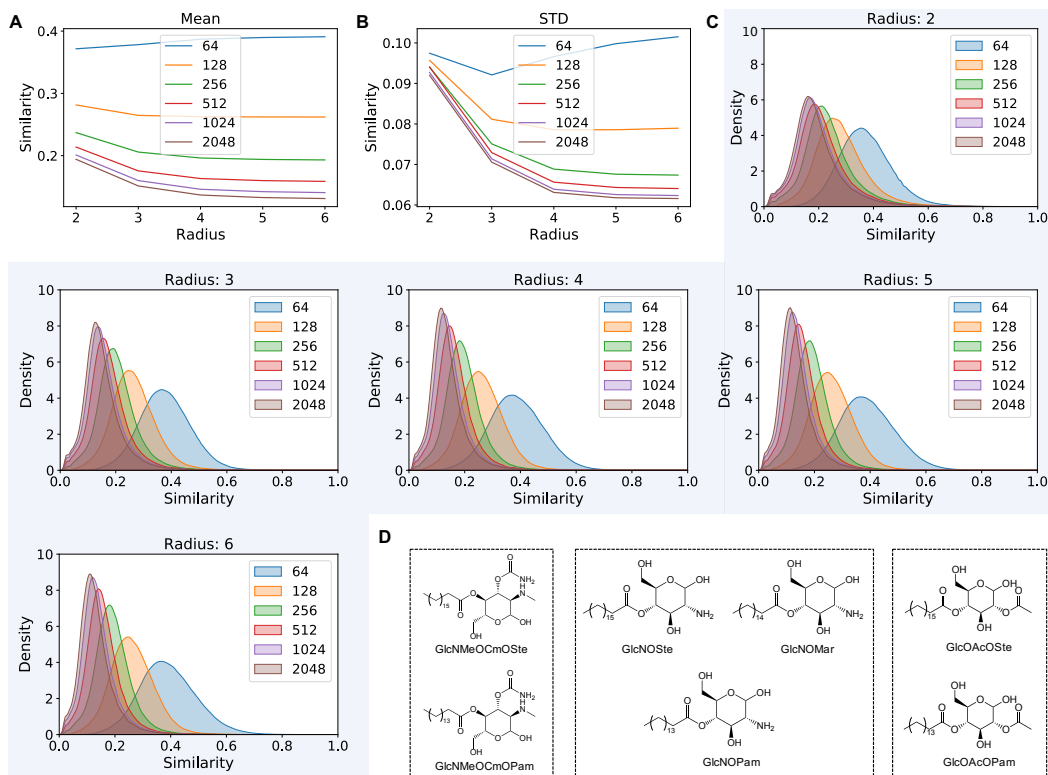


Figure A.17: **A.** Mean, **B.** standard deviation and **C.** distribution of Tanimoto similarity of all monomers in the glycans dataset, calculated using stereochemical extended connectivity fingerprints of different radii and bits. **D.** Glycans in the same box have the exact fingerprint for radius 3 and 128 bits.

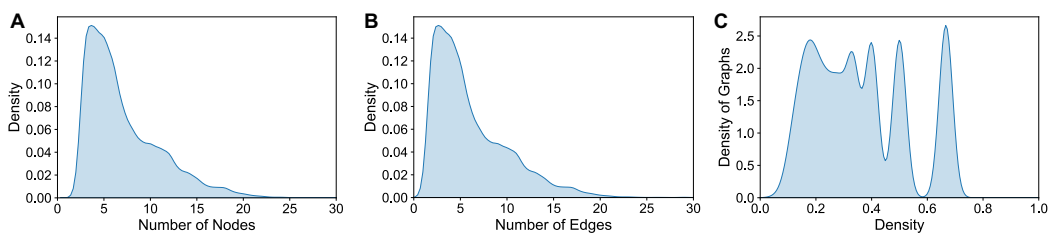


Figure A.18: Distribution of number of **A.** nodes, **B.** edges and **C.** density for glycan graphs.

E.2 SIMILARITY MATRIX

We computed the $(n \times n)$ similarity matrix for all glycans with labels on at least one taxonomic level using propagation attribute kernel in GraKeL (Figure A.18) (Siglidis et al., 2020). Each pair of graph similarity was computed for a maximum of 100 iterations. This resulted in 5% of the pairs being assigned a 0 similarity (10% of all indices in the similarity matrix are 0).

It may be noted that the computation of similarity using graph kernels is way more accessible than graph edit distances. The current computation was done on in minutes (wall time), parallelized across 24 cores. From visual inspection using htop, only about 30% of 24 cores were being used at any particular time, and less than 5% of all other cores were used, although there were 24 jobs running in parallel.

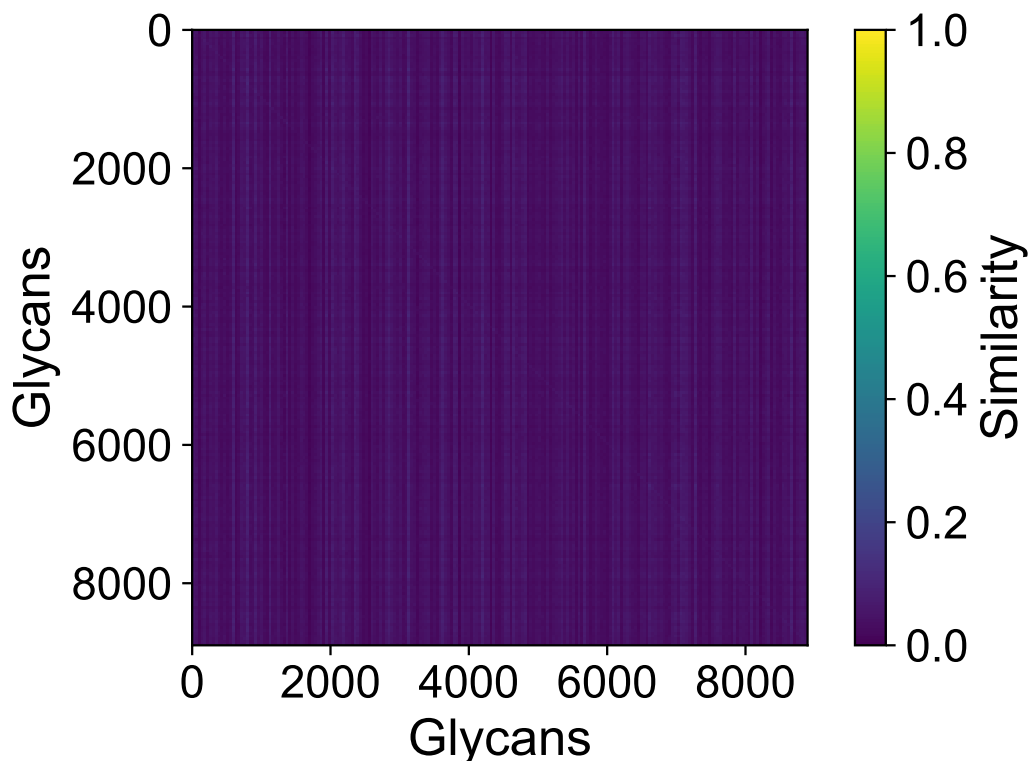


Figure A.19: 2D plot for the $(n \times n)$ similarity matrix of glycans. This is not symmetric because each row is normalized by its maximum.

E.3 DISSIMILARITY COMPUTATION USING EXACT GRAPH EDIT DISTANCES

We performed a grid search over combinations of possible node/edge substitution costs and multipliers for node/edge insertion/deletion costs to find an optimal set of values. Instead of similarity, we use the opposite – dissimilarity – as it is more intuitive when compared to a baseline case. We use the representative glycans in Figure 2B for this experiment, and present them here in Figure A.20 with the names we use in Table A.1.

For node/edge substitution, the Tanimoto distance between the stereochemical fingerprints, a value in the range of 0 and 1 (where 0 is a perfect match), is multiplied by the substitution cost to obtain the final graph edit distance. For node/edge insertion/deletion, a constant value which is the node/edge insertion/deletion is added to the graph edit distance. The baseline case where the edit distance is calculated for the macromolecule with itself is 0.

E.4 SIMILARITY COMPUTATION USING GRAPH KERNELS

We performed a grid search over hyperparameters of propagation attribute kernel – bin width 1, 3, 10, 100, and the preserved distance metric on local sensitive hashing ‘L1-norm’, ‘L2-norm’. We used 30 as the maximum number of iterations for the kernel computation for this experiment. We use the representative glycans Figure A.20, and present the results in Table A.2.

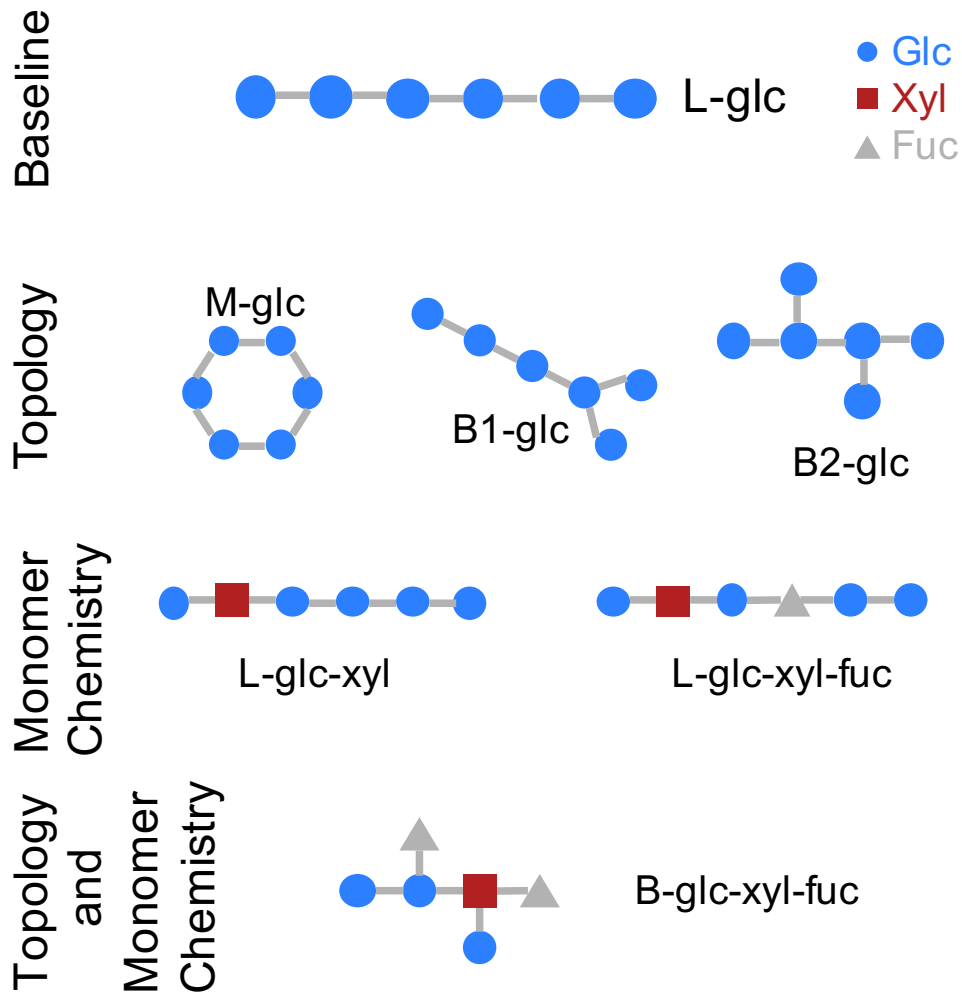


Figure A.20: Representative glycans used in the hyperparameter search for dissimilarity computation using exact graph edit distances, and similarity computation using graph kernels.

Table A.1: Dissimilarities computed using exact graph edit distances using different node/edge insertion/deletion and substitution multipliers. The remarks column notes down the hyperparameters, and baseline and other classes of glycans. Abbreviations - Hparam: hyperparameter, L: linear, B: branched, glc: glucose, xyl: xylose, fuc: fucose.

Remarks	Hyperparameters/Glycans	Cases															
HParam1	Insertion/Deletion Cost	1	1	1	1	3	3	3	3	5	5	5	5	10	10	10	10
HParam2	Substitution Cost	1	3	5	10	1	3	5	10	1	3	5	10	1	3	5	10
Baseline	L-glc	0	0	0	0	0	0	0	0	0	0	0	0	0	0	0	0
Topology	M-glc	1	1	1	1	3	3	3	3	5	5	5	5	10	10	10	10
	B1-glc	2	2	2	2	6	6	6	6	10	10	10	10	20	20	20	20
	B2-glc	4	4	4	4	12	12	12	12	20	20	20	20	40	40	40	40
Monomer Chemistry	L-glc-xyl	0.68	6	6	6	0.68	2.05	3.42	18	0.68	2.05	3.42	6.84	0.68	2.05	3.42	6.84
	L-glc-xyl-fuc	1.43	12	12	12	1.43	4.28	7.13	36	1.43	4.28	7.13	14.26	1.43	4.28	7.13	14.26
Topology and Chemistry	B-glc-xyl-fuc	6.17	14	14	14	14.17	18.5	22.84	42	22.17	26.5	30.84	41.67	42.17	46.5	50.84	61.67

Table A.2: Similarities computed using graph kernels with different values of bin width and distance metric. The remarks column notes down the hyperparameters, and baseline and other classes of glycans. Abbreviations - Hparam: hyperparameter, L: linear, B: branched, glc: glucose, xyl: xylose, fuc: fucose.

Remarks	Hyperparameters/Glycans	Cases							
HParam1	Bin width	1	1	3	3	10	10	100	100
HParam2	Distance metric	L1	L2	L1	L2	L1	L2	L1	L2
Baseline	L-glc	230	230	230	230	230	230	230	230
Topology	M-glc	61	61	61	61	61	61	61	61
	B1-glc	56	56	56	56	56	56	56	56
	B2-glc	51	51	51	51	51	51	51	51
Monomer Chemistry	L-glc-xyl	50	50	50	50	50	55	56	61
	L-glc-xyl-fuc	39	39	39	39	45	44	51	61
Topology and Chemistry	B-glc-xyl-fuc	23	23	23	23	35	33	46	51

F DIMENSIONALITY REDUCTION

F.1 HYPERPARAMETER OPTIMIZATION FOR UNIFORM MANIFOLD APPROXIMATION AND PROJECTION (UMAP)

Number of neighbors was optimized for 2-component UMAP dimensionality reduction of similarity vectors (Figure A.21) (McInnes et al., 2018). From visual inspection, UMAP with 128 neighbors seems to resolve into optimal size and number of clusters. The subplot shows distinct regions for the immunogenic and non-immunogenic glycans. We note that there is more to similarity than graph kernel distances, and observe that it has been effectively captured using the GNN models (Appendix G).

UMAP dimensionality reduction for higher number of components does not provide more information. The 3 components UMAP looked similar to the 2 components, with slightly more disentangled families (Figure A.22). We limited our visual analysis to 3 components. To check if more components can help in finding distinct clusters, we did dimensionality reduction for $\{2, 3, 5, 10, 30, 50\}$ components and let HDBSCAN - an unsupervised clustering algorithm - to figure out how many clusters are there (McInnes et al., 2017). We noted that the number of clusters are pretty similar, and in low 400s (Figure A.23). The high number of clusters indicates the diversity of the space, and the differences in terms of taxonomy. As a further check to see if the distribution of glycans in different clusters is different, we plotted the histograms of the glycans assigned to each cluster. Across all the components, the histograms seem to be consistent with the number of glycans in each of them (Figure A.24).

F.2 T-SNE BENCHMARK

We benchmarked the dimensionality reduction results obtained from UMAP against a broad range of t-stochastic neighbor embeddings (t-SNE) models (Van Der Maaten & Hinton, 2008). For the different models, we varied perplexity as $\{2, 5, 30, 50, 100\}$, and number of steps as $\{500, 1000, 5000\}$. From the scatter plot, colored by immunogenicity labels, we noted that dimensionality reduction using t-SNE was not able to deduce the differences and getting the glycans into distinct areas (Figure A.25).

G SUPERVISED LEARNING WITH GRAPH NEURAL NETWORKS

G.1 DEEP GRAPHS LIBRARY (DGL) GRAPHS

Following featurization, NetworkX graphs were converted into undirected, unweighted, and homogenous DGL graphs (Wang et al., 2019). For GCN and GAT model architectures, self-loops

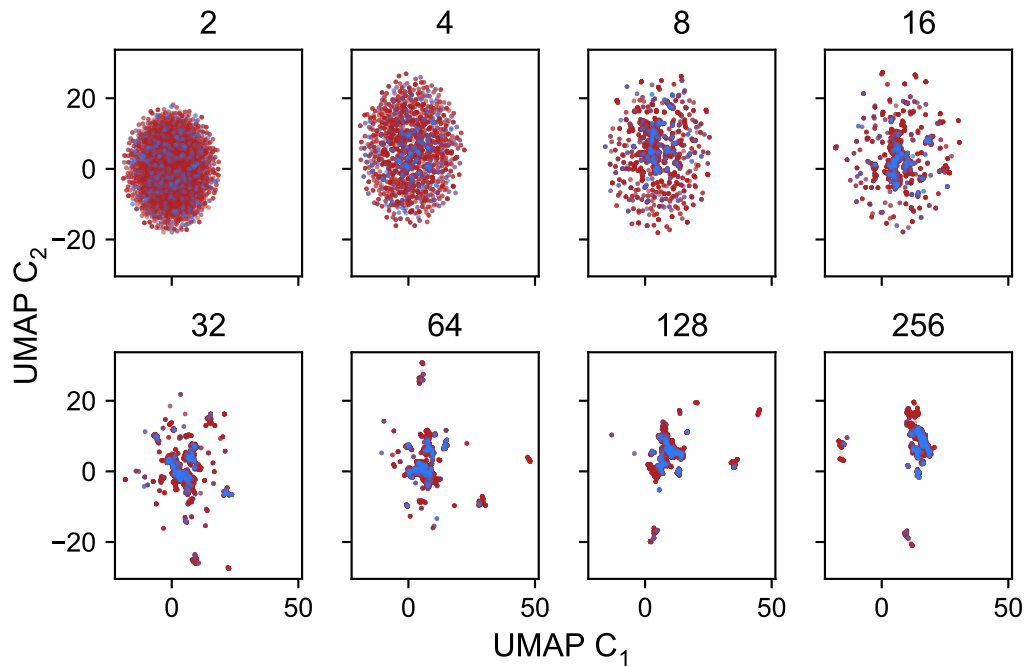


Figure A.21: Visualization of scatter plots for UMAP components, obtained by dimensionality reduction of similarity vectors. The number of neighbors for each UMAP computation has been noted in the title of the respective sub-plot. Coloration is by immunogenicity (red: immunogenic, blue: non-immunogenic glycan).

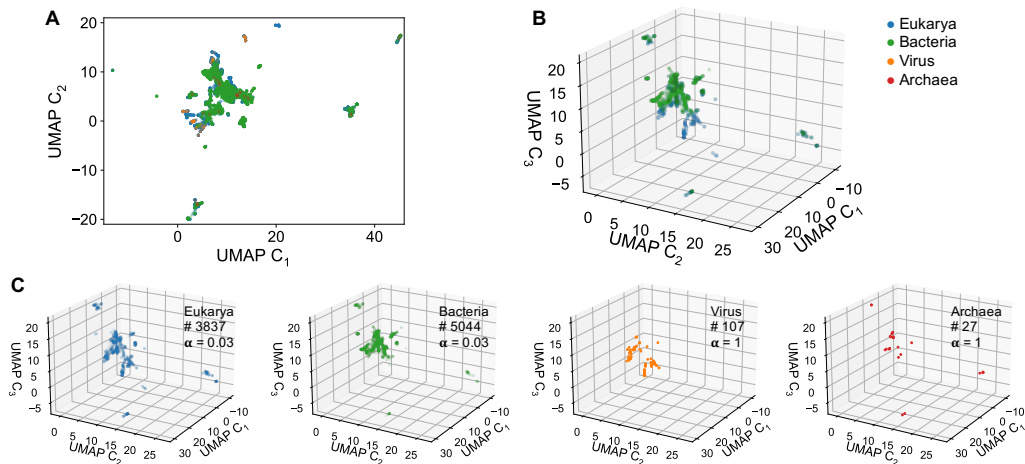


Figure A.22: Visualization of **A.** 2 and **B.** 3 components UMAP, colored by domain. **C.** Glycans corresponding to individual domains are shown, with the text noting the domain, number of glycans, and transparency (α) of each point on a scale of 0 to 1, where 1 is opaque

were added to the DGL graphs to prevent silent performance regression due to zero-in-degree nodes during training.

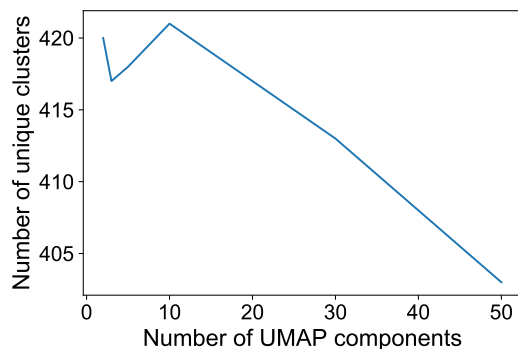


Figure A.23: Number of HDBSCAN unsupervised clusters obtained from UMAP dimensionality reduction for different components.

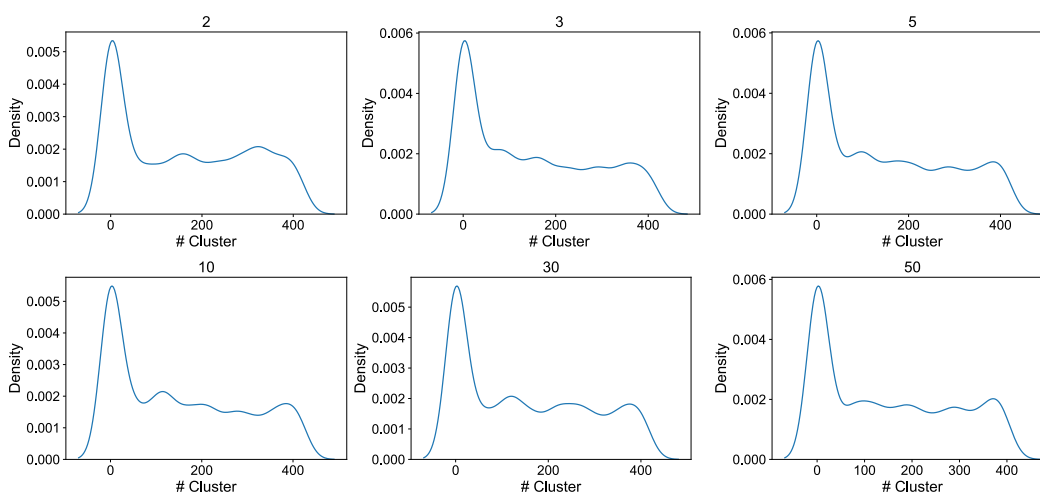


Figure A.24: Distribution of glycans in each cluster for HDBSCAN unsupervised clusters obtained from UMAP dimensionality reduction for different components. The components have been noted as titles for the sub-plots.

G.2 MODEL ARCHITECTURES

We performed graph classification using five distinct graph neural network model architectures detailed below:

- Weave (Kearnes et al., 2016)
- Message Passing Neural Networks (MPNNs) (Gilmer et al., 2017)
- Attentive FP (Xiong et al., 2020)
- Graph convolutional networks (GCN) (Kipf & Welling, 2019)
- Graph Attention Networks (GAT) (Velickovic et al., 2017)

While Weave, MPNN, and Attentive FP utilize both node and edge attributes in prediction, GCN and GAT only consider node attributes. The models were trained using implementations in the DGL LifeSci library (Wang et al., 2019). For classification, the optimization was done by minimization of average cross-entropy loss between batches and additional metrics such as F1 score, recall, precision and accuracy were noted. For regression, the optimization was done by minimization of root-mean-squared-error loss on the validation dataset.

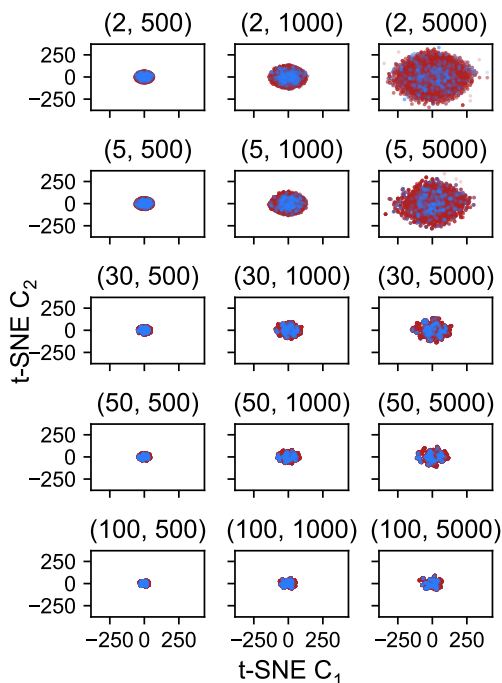


Figure A.25: Visualization of scatter plots for t-SNE components, obtained by dimensionality reduction of similarity vectors. The (perplexity, number of steps) for each t-SNE computation has been noted in the title of the respective sub-plot. Coloration is by immunogenicity (red: immunogenic, blue: non-immunogenic glycans).

G.3 GLYCAN GRAPHS CLASSIFICATION

G.3.1 IMMUNOGENICITY

Dataset. 1313 glycans in the database have immunogenicity labels, 631 of which are immunogenic and 682 of which are not immunogenic. The training was performed on 60%, validated on 20%, and tested on held-out 20% data.

Models. We classified immunogenicity using 5 model architectures combined with 2 different node and edge featurization types, for a total of 10 model architecture-attribute pairs. For each benchmark, hyperparameter optimization against minimization of binary cross entropy loss was performed on SigOpt, a standardized hyperparameter optimization platform, for 1000 observations and the 5 best sets of hyperparameters were extracted. Each model architecture and featurization combination was trained using the 5 best sets of hyperparameters from SigOpt using 5 distinct random seeds for splitting the dataset into train-validation-test datasets, for a total of 25 trainings per model per attribute type. The tables below report the metrics for the most optimal set of hyperparameters, the values of the most optimal hyperparameters, and mean metrics for each training across all 25 runs. All models achieve stellar performance on all metrics, with little meaningful difference in performance between fingerprint and one-hot encoding featurization (Figures A.26-A.28 ; Table A.3).

G.3.2 TAXONOMY

Dataset. The taxonomy of the glycans was considered on eight levels: domain, kingdom, phylum, class, order, genus, and species. First, the classification of each species into the other seven taxonomic levels was obtained from the supplementary tables of SweetOrigins (Bojar et al., 2021). For each glycan with species information, taxonomic information was added in a new .csv file, with multiple labels on the same taxonomic level separated by commas. Afterwards, any labels with fewer than five glycans were removed, and any species names ending with “sp” that are therefore genus

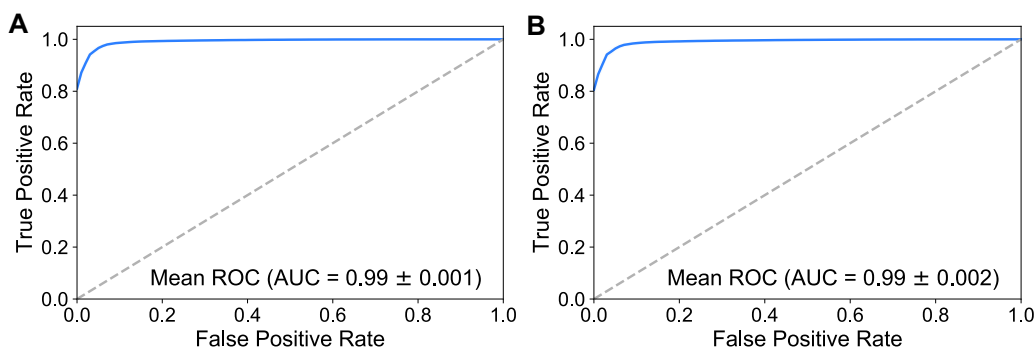


Figure A.26: ROC-AUC curves for fingerprint and one-hot encoding-featurized graphs. **A.** Mean ROC-AUC curve of all 25 fingerprint-featurized experiments (5 model architectures with 5 sets of hyperparameters for each architecture), with the standard deviation shaded in light blue too insignificant to be visible in the graph. **B.** Mean ROC-AUC curve of all 25 one-hot encoding-featurized experiments.

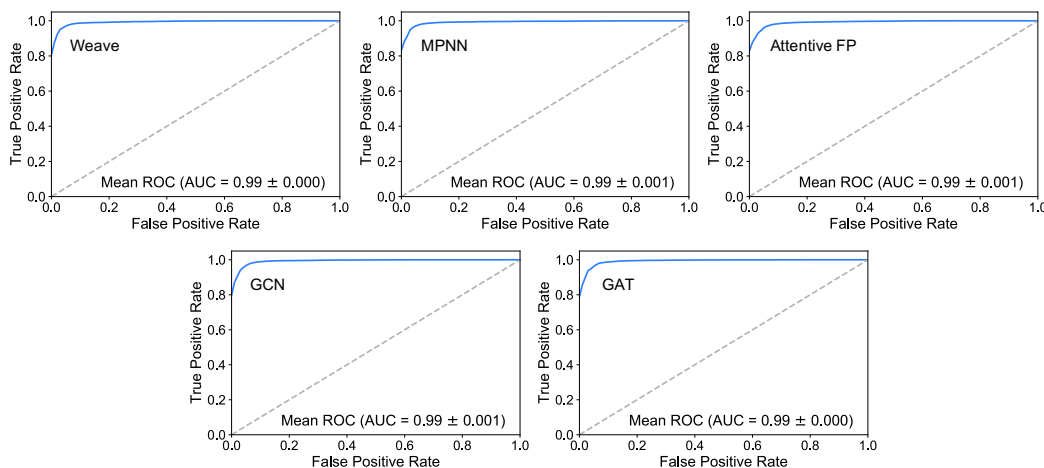


Figure A.27: Mean ROC-AUC curves for fingerprint-featurized experiments for each of the five model architectures (Weave, MPNN, Attentive FP, GCN, and GAT), with the standard deviation shaded in light blue too insignificant to be visible. A standard deviation of 0.000 denotes a value of <0.001 .

labels in disguise were filtered out to produce the final dataset for taxonomic training. The final dataset consists of 8899 unique glycans with labels on at least one taxonomic level encompassing 4 domains, 9 kingdoms, 33 phyla, 70 classes, 144 orders, 253 families, 400 genus, and 567 species. The training was performed on 60%, validated on 20%, and tested on held-out 20% data.

Graph labels were generated as one-hot encodings for each taxonomic level, with the length of each one-hot encoding tensor corresponding with the number of unique labels in the taxonomic level. The taxonomy labels accommodate cases in which glycans possess multiple labels within the same taxonomic level.

Models. Benchmarks of multi-label classification were performed using a similar process as with immunogenicity classification for 5 different model architectures, 2 different node and edge attribution types, and 8 different taxonomic levels for a total of 80 model architecture–attribute–taxonomic level combination. For each combination, hyperparameter optimization against minimization of binary cross entropy loss was performed on SigOpt for 1000 observations and the 5 best sets of

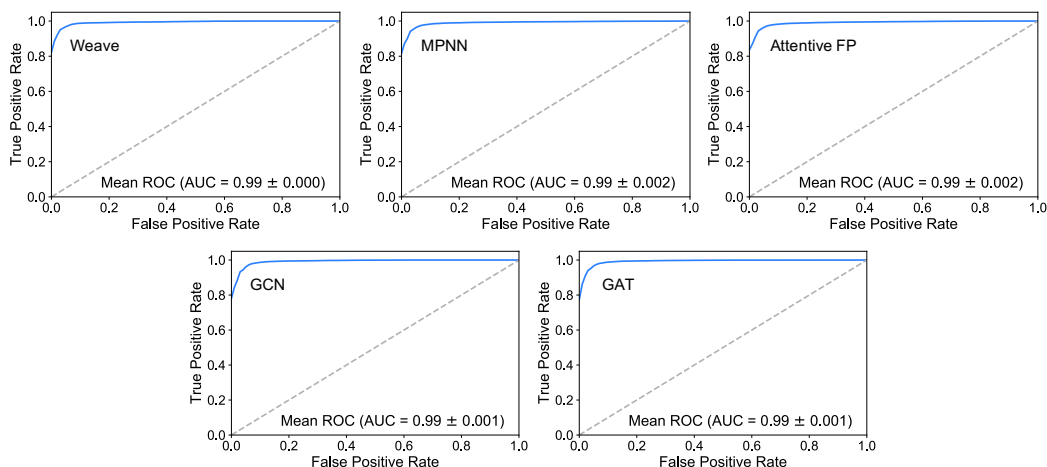


Figure A.28: Mean ROC-AUC curves for one-hot encoding-featurized experiments for each of the five model architectures (Weave, MPNN, Attentive FP, GCN, and GAT), with the standard deviation shaded in light blue too insignificant to be visible. A standard deviation of 0.000 denotes a value of <0.001 .

Table A.3: Test dataset metrics for the most optimal set of hyperparameters, or the set of hyperparameters that results in the lowest loss. For each metric, the mean μ and standard deviation σ are displayed across all 5 random seeds. “FP” denotes condensed fingerprint featurization, and “One-hot” denotes one-hot encoding featurization.

Model	Attribute Type	ROC-AUC		F1		Recall		Precision		Accuracy		Loss	
		μ	σ	μ	σ	μ	σ	μ	σ	μ	σ	μ	σ
Weave	FP	0.990	0.005	0.956	0.011	0.955	0.012	0.957	0.011	0.956	0.011	0.133	0.106
	One-hot	0.992	0.005	0.962	0.007	0.962	0.007	0.962	0.007	0.962	0.007	0.105	0.055
MPNN	FP	0.985	0.009	0.955	0.012	0.955	0.012	0.957	0.012	0.955	0.012	0.137	0.100
	One-hot	0.988	0.006	0.953	0.010	0.953	0.010	0.954	0.010	0.953	0.010	0.123	0.052
AttentiveFP	FP	0.990	0.005	0.954	0.011	0.953	0.011	0.955	0.012	0.954	0.011	0.125	0.104
	One-hot	0.990	0.005	0.951	0.011	0.951	0.012	0.952	0.011	0.952	0.011	0.120	0.084
GCN	FP	0.992	0.004	0.953	0.013	0.953	0.013	0.954	0.012	0.953	0.012	0.110	0.086
	One-hot	0.990	0.006	0.955	0.012	0.956	0.012	0.956	0.013	0.956	0.012	0.123	0.110
GAT	FP	0.991	0.006	0.954	0.014	0.954	0.013	0.954	0.014	0.954	0.014	0.109	0.081
	One-hot	0.991	0.004	0.954	0.011	0.954	0.011	0.955	0.010	0.955	0.011	0.119	0.085

hyperparameters were extracted. Each model architecture, featurization, and taxonomic level combination was trained using the 5 best sets of hyperparameters from SigOpt using 5 distinct random seeds for splitting the dataset into train-validation-test datasets, for a total of 25 trainings per combination. The pipeline and models achieve state-of-the-art performance on multilabel taxonomic classification on all taxonomic levels (Figures A.29-A.36, Table A.4). Additional supplementary tables display the validation and test metrics for the most optimal set of hyperparameters, the values of the most optimal hyperparameters, and mean test metrics for each training across all 25 runs (Supplementary Tables 1-2).

Table A.4: The most optimal model architecture and node/edge attribute type that results in the lowest loss for prediction of all taxonomic levels. For each metric, the mean μ and standard deviation σ are displayed across all 5 random seeds. “FP” denotes condensed fingerprint featurization, and “One-hot” denotes one-hot encoding featurization.

Taxonomic Level	Model, Attribute Type	ROC-AUC		F1		Recall		Precision		Accuracy		Loss		Hamming Loss	
		μ	σ	μ	σ	μ	σ	μ	σ	μ	σ	μ	σ	μ	σ
Domain	Attentive FP, FP	0.993	0	0.938	0.002	0.935	0.004	0.941	0.001	0.925	0.001	0.087	0.002	0.03	0.001
Kingdom	Attentive FP, FP	0.994	0	0.912	0.001	0.891	0.003	0.934	0.002	0.892	0.005	0.056	0.003	0.019	0
Phylum	GCN, FP	0.99	0	0.84	0.009	0.8	0.011	0.885	0.009	0.802	0.01	0.029	0.001	0.009	0
Class	GCN, FP	0.986	0.001	0.741	0.008	0.666	0.01	0.836	0.006	0.67	0.009	0.022	0	0.007	0
Order	GCN, FP	0.979	0.001	0.638	0.012	0.541	0.023	0.778	0.018	0.548	0.016	0.017	0	0.004	0
Family	GAT, FP	0.975	0.003	0.557	0.015	0.456	0.017	0.715	0.015	0.469	0.019	0.013	0	0.003	0
Genus	GCN, One-hot	0.963	0.003	0.513	0.015	0.397	0.015	0.723	0.020	0.412	0.010	0.009	0	0.002	0
Species	GCN, FP	0.968	0.003	0.487	0.021	0.382	0.031	0.675	0.018	0.395	0.020	0.007	0	0.002	0

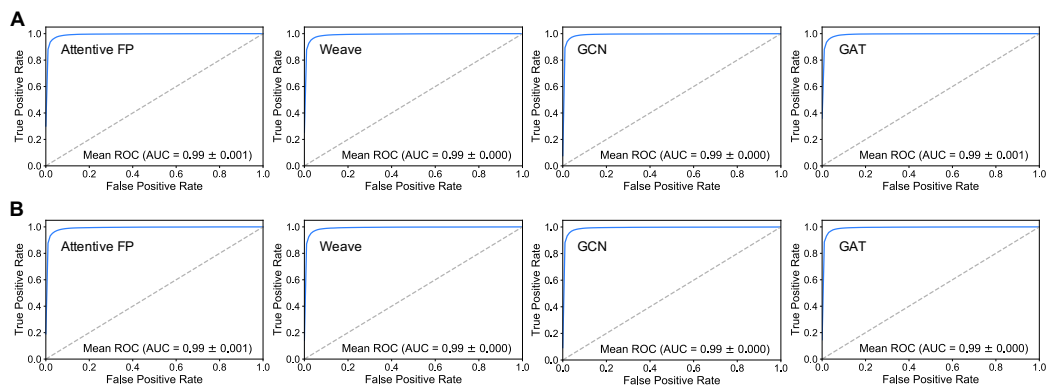


Figure A.29: ROC-AUC curves for classification on the domain level for each of four model architectures (Weave, Attentive FP, GCN, and GAT), with the standard deviation shaded in light blue too insignificant to be visible. A standard deviation of 0.000 denotes a value of <0.001 . **A.** Mean ROC-AUC curves for fingerprint-featurized experiments, with each graph displaying the mean and standard deviation across 5 sets of hyperparameters. **B.** Mean ROC-AUC curves for one-hot encoding-featurized experiments.

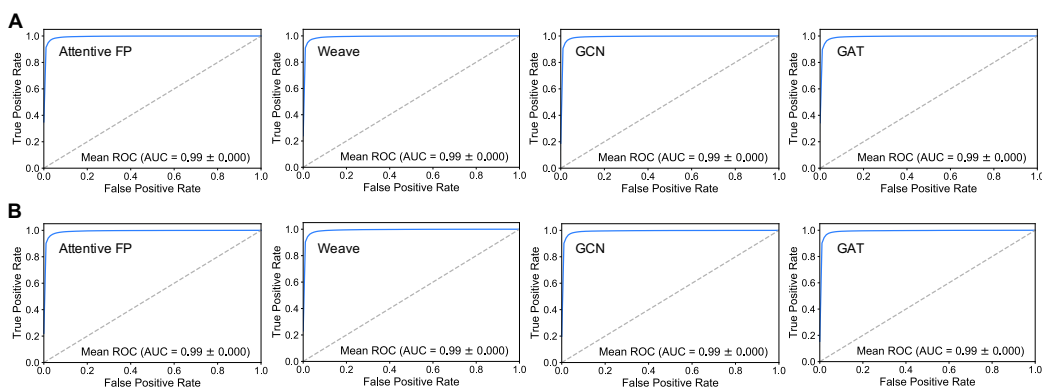


Figure A.30: ROC-AUC curves for classification on the kingdom level for each of four model architectures (Weave, Attentive FP, GCN, and GAT), with the standard deviation shaded in light blue too insignificant to be visible. A standard deviation of 0.000 denotes a value of <0.001 . **A.** Mean ROC-AUC curves for fingerprint-featurized experiments, with each graph displaying the mean and standard deviation across 5 sets of hyperparameters. **B.** Mean ROC-AUC curves for one-hot encoding-featurized experiments.

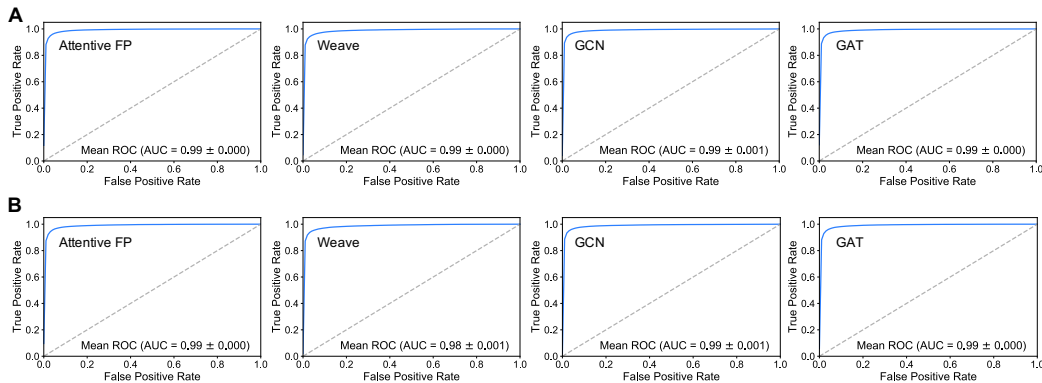


Figure A.31: ROC-AUC curves for classification on the phylum level for each of four model architectures (Weave, Attentive FP, GCN, and GAT), with the standard deviation shaded in light blue too insignificant to be visible. A standard deviation of 0.000 denotes a value of <0.001 . **A.** Mean ROC-AUC curves for fingerprint-featurized experiments, with each graph displaying the mean and standard deviation across 5 sets of hyperparameters. **B.** Mean ROC-AUC curves for one-hot encoding-featurized experiments.

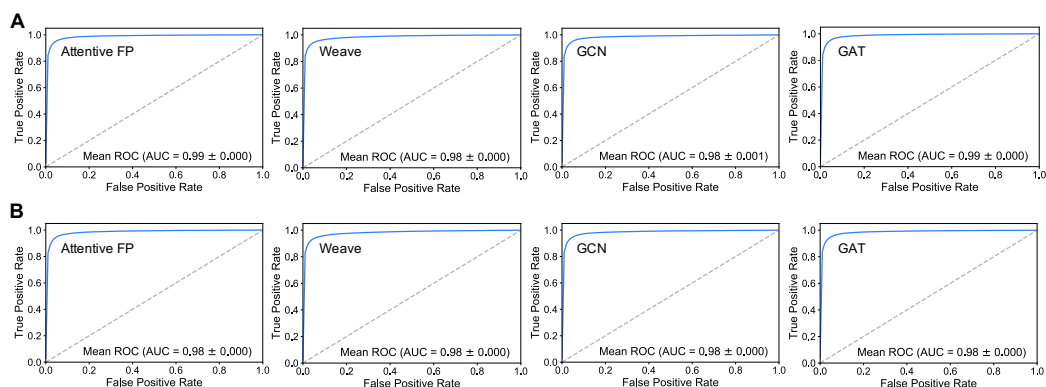


Figure A.32: ROC-AUC curves for classification on the class level for each of four model architectures (Weave, Attentive FP, GCN, and GAT), with the standard deviation shaded in light blue too insignificant to be visible. A standard deviation of 0.000 denotes a value of <0.001 . **A.** Mean ROC-AUC curves for fingerprint-featurized experiments, with each graph displaying the mean and standard deviation across 5 sets of hyperparameters. **B.** Mean ROC-AUC curves for one-hot encoding-featurized experiments.

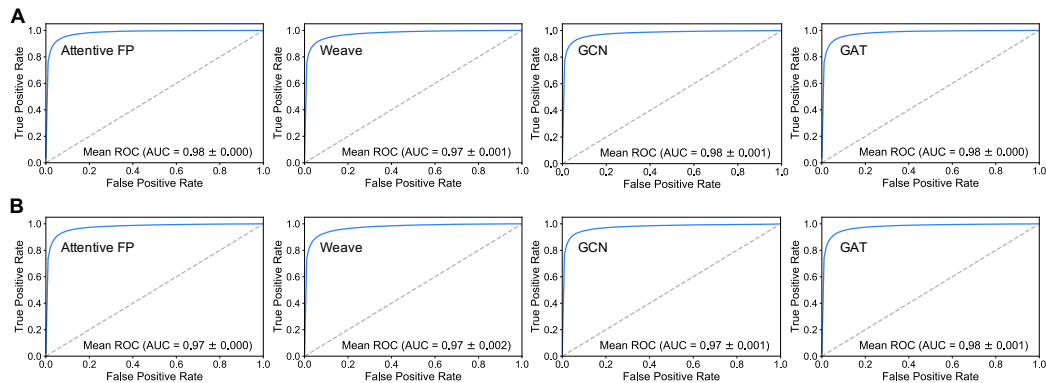


Figure A.33: ROC-AUC curves for classification on the order level for each of four model architectures (Weave, Attentive FP, GCN, and GAT), with the standard deviation shaded in light blue too insignificant to be visible. A standard deviation of 0.000 denotes a value of <0.001 . **A.** Mean ROC-AUC curves for fingerprint-featurized experiments, with each graph displaying the mean and standard deviation across 5 sets of hyperparameters. **B.** Mean ROC-AUC curves for one-hot encoding-featurized experiments.

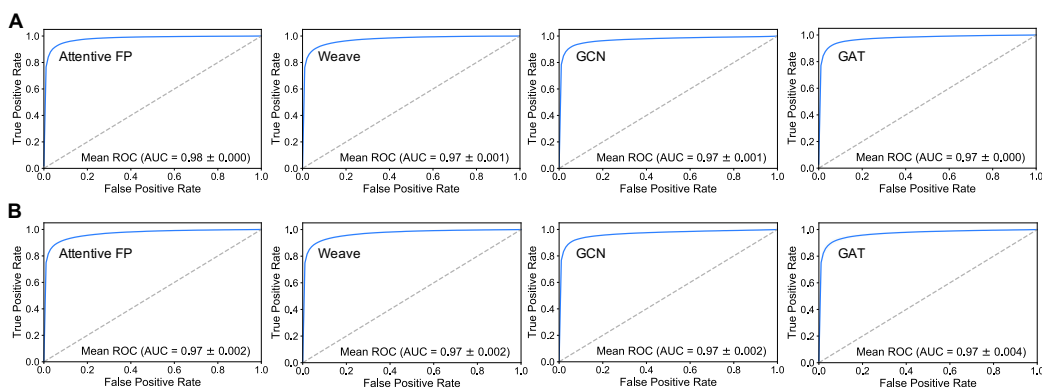


Figure A.34: ROC-AUC curves for classification on the family level for each of four model architectures (Weave, Attentive FP, GCN, and GAT), with the standard deviation shaded in light blue too insignificant to be visible. A standard deviation of 0.000 denotes a value of <0.001 . **A.** Mean ROC-AUC curves for fingerprint-featurized experiments, with each graph displaying the mean and standard deviation across 5 sets of hyperparameters. **B.** Mean ROC-AUC curves for one-hot encoding-featurized experiments.

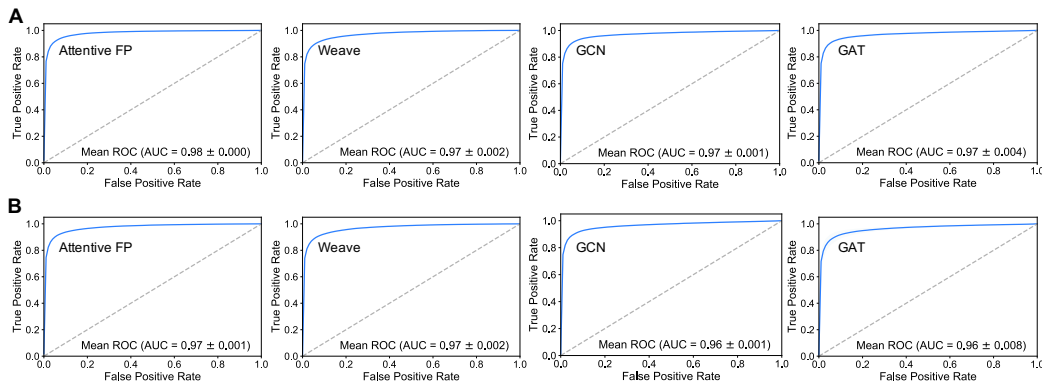


Figure A.35: ROC-AUC curves for classification on the genus level for each of four model architectures (Weave, Attentive FP, GCN, and GAT), with the standard deviation shaded in light blue too insignificant to be visible. A standard deviation of 0.000 denotes a value of <0.001 . **A.** Mean ROC-AUC curves for fingerprint-featurized experiments, with each graph displaying the mean and standard deviation across 5 sets of hyperparameters. **B.** Mean ROC-AUC curves for one-hot encoding-featurized experiments.

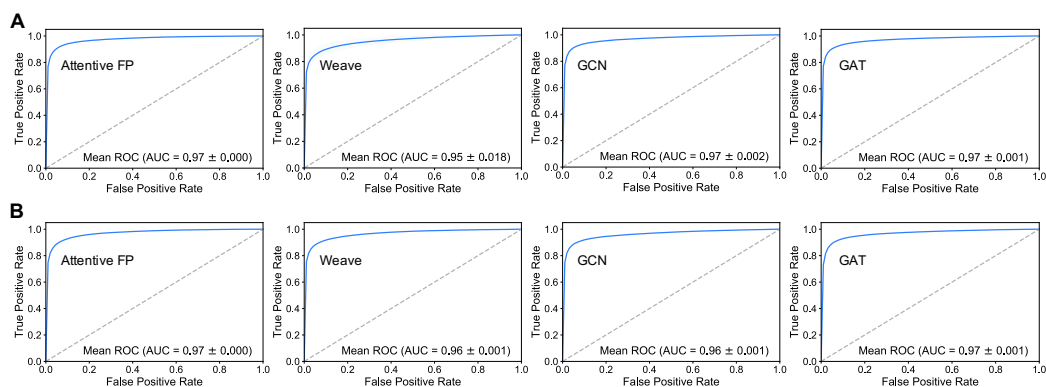


Figure A.36: ROC-AUC curves for classification on the species level for each of four model architectures (Weave, Attentive FP, GCN, and GAT), with the standard deviation shaded in light blue too insignificant to be visible. A standard deviation of 0.000 denotes a value of <0.001 . **A.** Mean ROC-AUC curves for fingerprint-featurized experiments, with each graph displaying the mean and standard deviation across 5 sets of hyperparameters. **B.** Mean ROC-AUC curves for one-hot encoding-featurized experiments.

G.4 BENCHMARKING TOP GNN MODELS AGAINST RESULTS REPORTED IN LITERATURE - GLYCANS

For the top-performing models in Tables A.3 and A.4, hyperparameter optimization on SigOpt was performed again using the same method as the benchmarks in the work by Burkholz et al. (2021): training on 80% of the dataset and reporting metrics on the remaining 20% used as a validation dataset (Table A.5). The experiment on SigOpt was optimized through minimization of the loss, and the remaining metrics (ROC-AUC, F1, recall, precision, and accuracy) were obtained as stored metrics in the SigOpt experiment. However, to obtain more robust metrics, we averaged across 25 models, instead of the 5 models in Burkholz et al. (2021). In 4 out of 8 tasks, the models presented in our work perform better, and are comparable for the rest 4.

G.5 PEPTIDE GRAPHS REGRESSION

Dataset. As explained in Appendix Section B.2, the overall peptides dataset was filtered into two sub-datasets, one for *E. coli* and one for *S. aureus*. The *E. coli* dataset contains 4,445 peptides, including 4330 monomers, 71 multimers, and 44 multi-peptides. The *S. aureus* dataset contains 3,686 peptides, including 3617 monomers, 61 multimers, and 8 multi-peptides. The training for prediction of the target activity, or antimicrobial concentration, of the peptides was performed on 60%, validated on 20%, and tested on held-out 20% data.

Models. We performed target activity regression using 5 model architectures combined with 2 different node and edge featurization types and 2 dataset normalization types, for a total of 20 model combinations for each of the two species. The 2 normalization methods were standard scaler and quantile transform from scikit-learn (Pedregosa et al., 2011). For each benchmark, hyperparameter optimization against minimization of root mean square error (RMSE) was performed on SigOpt (Clark & Hayes, 2019), for 500 observations and the 5 best sets of hyperparameters were extracted. Each model architecture and featurization combination was trained using the 5 best sets of hyperparameters from SigOpt using 5 distinct random seeds for splitting the dataset into train-validation-test datasets, for a total of 25 trainings per model combination. All models achieve stellar performance on all metrics, with little meaningful difference in performance between fingerprint and one-hot encoding featurization (Figures A.37-A.44, Appendix Table A.6). Additional supplementary tables display the validation and test metrics for the most optimal set of hyperparameters, the values of the most optimal hyperparameters, and mean test metrics for each training across all 25 runs (Supplementary Tables 3-4).

Table A.5: Validation metrics of the top-performing model architecture and attribute combinations for immunogenicity and taxonomic levels obtained from SigOpt using a 0.8, 0.2 train-validation split of the dataset. The subset accuracy values are compared directly with the results for augmented models presented in Table 1 of Burkholz et al. (2021). The higher value is bolded for each task. In 4 out of 8 tasks, the models presented in our work perform better, and are comparable for the rest 4.

Class	Paper	Model + Attribute Type	ROC-AUC	F1	Recall	Precision	Accuracy	CE Loss	Hamming Loss
Immunogenicity	This Work	Weave, one-hot	0.999	0.989	0.989	0.989	0.989	0.018	-
	Burkholz, et. al.	-	-	-	-	-	0.942	0.149	-
Domain	This Work	Attentive FP, fp	0.994	0.946	0.941	0.951	0.935	0.081	0.027
	Burkholz, et. al.	-	-	-	-	-	0.939	0.181	-
Kingdom	This Work	Attentive FP, fp	0.997	0.936	0.895	0.922	0.921	0.043	0.014
	Burkholz, et. al.	-	-	-	-	-	0.907	0.301	-
Phylum	This Work	GCN, fp	0.991	0.845	0.806	0.889	0.808	0.029	0.009
	Burkholz, et. al.	-	-	-	-	-	0.841	0.603	-
Class	This Work	GCN, FP	0.987	0.776	0.713	0.850	0.718	0.021	0.006
	Burkholz, et. al.	-	-	-	-	-	0.745	0.976	-
Order	This Work	GCN, fp	0.979	0.638	0.541	0.778	0.548	0.017	0.004
	Burkholz, et. al.	-	-	-	-	-	0.582	1.728	-
Family	This Work	GAT, fp	0.984	0.617	0.525	0.748	0.542	0.011	0.003
	Burkholz, et. al.	-	-	-	-	-	0.535	2.051	-
Genus	This Work	GCN, fp	0.975	0.546	0.453	0.688	0.456	0.009	0.002
	Burkholz, et. al.	-	-	-	-	-	0.475	2.320	-
Species	This Work	GCN, fp	0.976	0.510	0.403	0.694	0.438	0.007	0.002
	Burkholz, et. al.	-	-	-	-	-	0.428	2.505	-

Table A.6: The most optimal model architecture, node/edge attribute type, and normalization method that results in the lowest RMSE for target activity regression. For each metric, the mean μ and standard deviation σ are displayed across all 5 random seeds. “FP” denotes condensed fingerprint featurization, and “One-hot” denotes one-hot encoding featurization.

Species	Model, Attribute, Normalization Type	Pearson r2		MAE		RMSE		Spearman r		Kendall’s Tau		Loss	
		μ	σ	μ	σ	μ	σ	μ	σ	μ	σ	μ	σ
<i>E. coli</i>	Weave, FP, Quantile transform	0.465	0.023	0.166	0.004	0.212	0.006	0.68	0.019	0.501	0.014	0.023	0.002
<i>S. aureus</i>	GCN, One-hot, Quantile transform	0.38	0.032	0.185	0.008	0.229	0.007	0.62	0.027	0.451	0.023	0.026	0.002

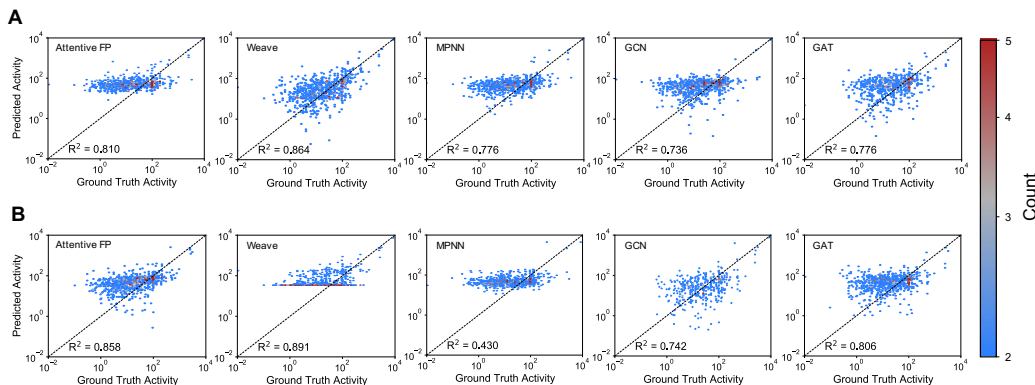


Figure A.37: Parity plots for *Escherichia coli* validation dataset normalized with standard scaler for regression of peptide target activity for each of five model architectures (Attentive FP, Weave, MPNN, GCN, and GAT), all using the same train-validation-test dataset split. **A.** Parity plots for fingerprint-featurized experiments, with each graph displaying the top set of hyperparameters. **B.** Parity plots for one-hot encoding-featurized experiments, with each graph displaying the top set of hyperparameters.

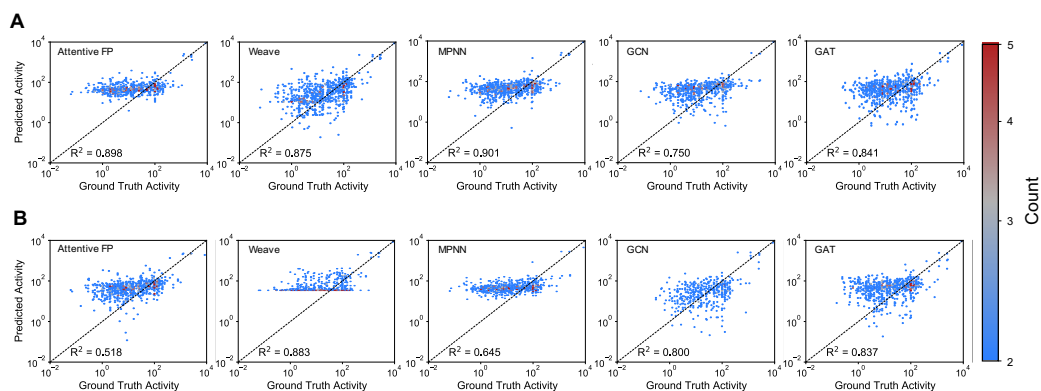


Figure A.38: Parity plots for *Escherichia coli* test dataset normalized with standard scaler for regression of peptide target activity for each of five model architectures (Attentive FP, Weave, MPNN, GCN, and GAT), all using the same train-validation-test dataset split. **A.** Parity plots for fingerprint-featurized experiments, with each graph displaying the top set of hyperparameters. **B.** Parity plots for one-hot encoding-featurized experiments, with each graph displaying the top set of hyperparameters.

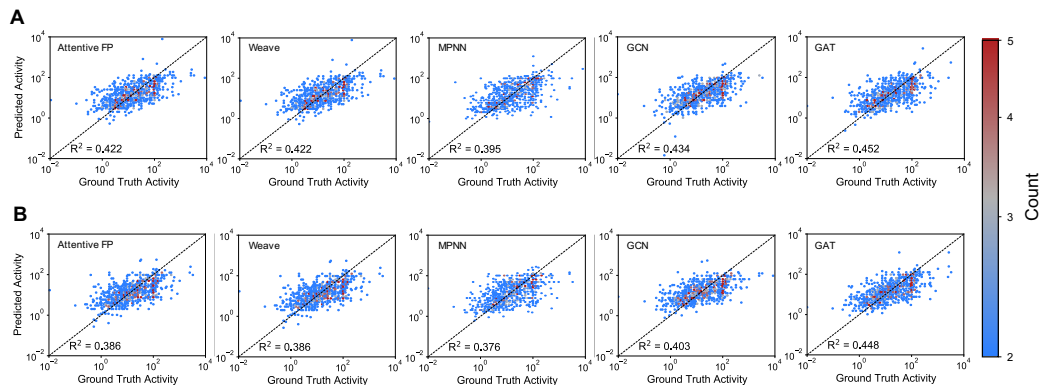


Figure A.39: Parity plots for *Escherichia coli* validation dataset normalized with quantile transform for regression of peptide target activity for each of five model architectures (Attentive FP, Weave, MPNN, GCN, and GAT). **A.** Parity plots for fingerprint-featurized experiments, each graph for the top set of hyperparameters and the same train-validation-test dataset split. **B.** Parity plots for one-hot encoding-featurized experiments, each graph for the top set of hyperparameters and the same train-validation-test dataset split.

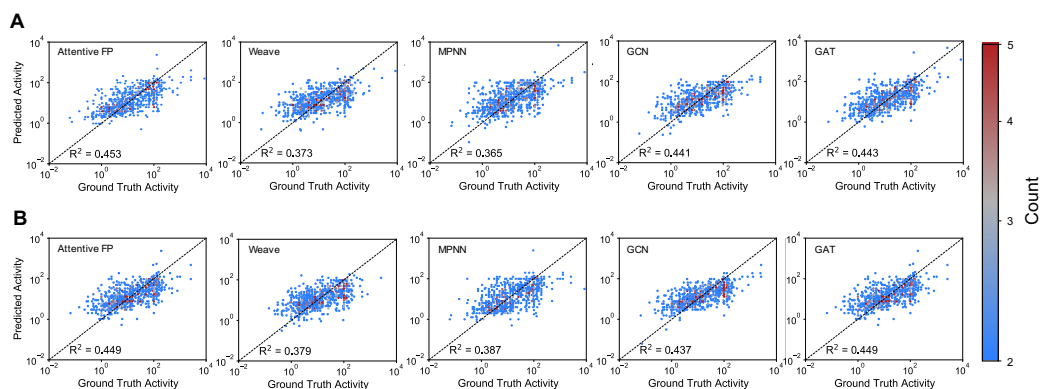


Figure A.40: Parity plots for *Escherichia coli* test dataset normalized with quantile transform for regression of peptide target activity for each of five model architectures (Attentive FP, Weave, MPNN, GCN, and GAT). **A.** Parity plots for fingerprint-featurized experiments, each graph for the top set of hyperparameters with the same train-validation-test dataset split across all plots. **B.** Parity plots for one-hot encoding-featurized experiments, each graph for the top set of hyperparameters with the same train-validation-test dataset split across all plots.

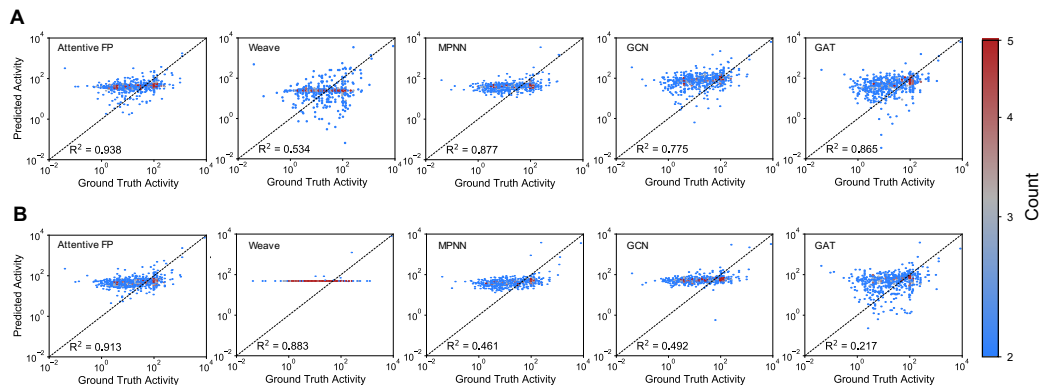


Figure A.41: Parity plots for *Staphylococcus aureus* validation dataset normalized with standard scaler for regression of peptide target activity for each of five model architectures (Attentive FP, Weave, MPNN, GCN, and GAT). **A.** Parity plots for fingerprint-featurized experiments, each graph for the top set of hyperparameters with the same train-validation-test dataset split across all plots. **B.** Parity plots for one-hot encoding-featurized experiments, each graph for the top set of hyperparameters with the same train-validation-test dataset split across all plots.

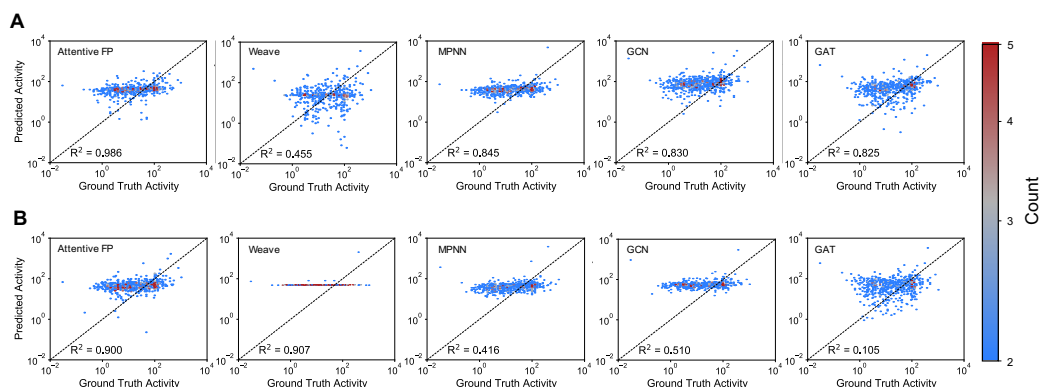


Figure A.42: Parity plots for *Staphylococcus aureus* test dataset normalized with standard scaler for regression of peptide target activity for each of five model architectures (Attentive FP, Weave, MPNN, GCN, and GAT). **A.** Parity plots for fingerprint-featurized experiments, each graph for the top set of hyperparameters with the same train-validation-test dataset split across all plots. **B.** Parity plots for one-hot encoding-featurized experiments, with each graph displaying the top set of hyperparameters with the same train-validation-test dataset split across all plots.

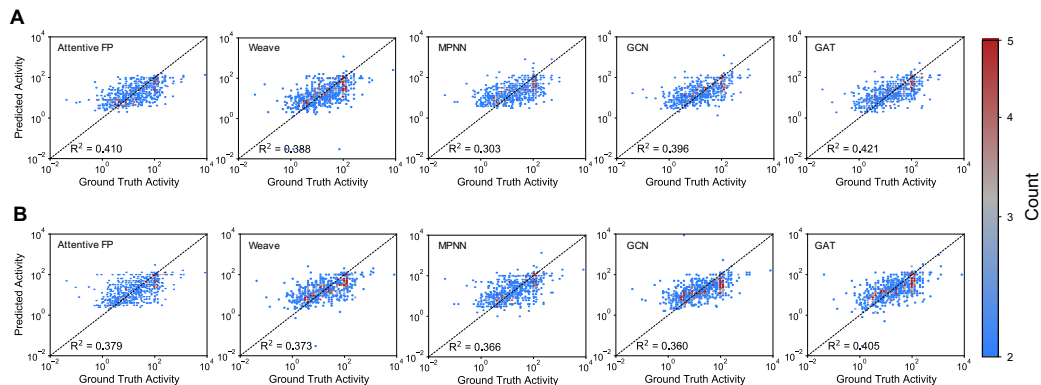


Figure A.43: Parity plots for *Staphylococcus aureus* validation dataset normalized with quantile transform for regression of peptide target activity for each of five model architectures (Attentive FP, Weave, MPNN, GCN, and GAT). **A.** Parity plots for fingerprint-featurized experiments, each graph for the top set of hyperparameters with the same train-validation-test dataset split across all plots. **B.** Parity plots for one-hot encoding-featurized experiments, each graph for the top set of hyperparameters with the same train-validation-test dataset split across all plots.

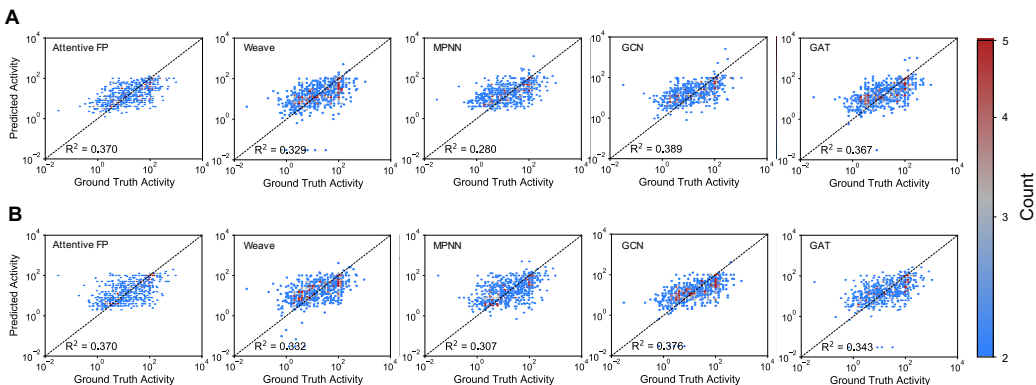


Figure A.44: Parity plots for *Staphylococcus aureus* test dataset normalized with quantile transform for regression of peptide target activity for each of five model architectures (Attentive FP, Weave, MPNN, GCN, and GAT). **A.** Parity plots for fingerprint-featurized experiments, each graph for the top set of hyperparameters with the same train-validation-test dataset split across all plots. **B.** Parity plots for one-hot encoding-featurized experiments, each graph for the top set of hyperparameters with the same train-validation-test dataset split across all plots.

H ATTRIBUTION ANALYSIS

H.1 SELECTION OF MODEL ARCHITECTURE - ATTRIBUTION METHOD

We used integrated gradients (IGs) (Sundararajan et al., 2017) and Input x Grad (InpGrad) (Shrikumar et al., 2017) for the attribution analysis of the GNNs - Weave, Attentive FP and MPNN. The model architecture selection was done to have one of each type of architecture – Weave (graph convolution), Attentive FP (graph attention), and MPNN (message passing).

The macromolecule is represented as a graph, $\mathcal{G}(V, E)$, where V represents monomers at vertices/nodes, and E represents connecting bonds at the edges.

IGs interpolate between the input graph and a baseline graph, where all features are zero, and accumulate the gradient values for each node (Equation 1). The notation follows (Sanchez-Lengeling et al., 2020).

$$\mathcal{G}_A = (\mathcal{G} - \mathcal{G}') \int_{\alpha=0}^1 \frac{dy(\mathcal{G}' + \alpha(\mathcal{G} - \mathcal{G}'))}{d\mathcal{G}} d\alpha \quad (1)$$

InpGrad is the element-wise product of the input graph and the gradient.

$$\mathcal{G}_A = \left(\frac{d\hat{y}}{d\mathcal{G}} \right)^T \mathcal{G} \quad (2)$$

For the attention-based GNN, AttentiveFP, in addition to IGs and InpGrad, we evaluated attribution using attention weights, where the node attention weights are obtained by averaging over the attention scores of the adjacent nodes.

For each attribution method, we obtained the node weights by multiplying the positive weights with the input fingerprint vectors -

$$\mathbf{n} = \sum_{nodes} \mathcal{G}_A^+ \mathcal{G}, \quad (3)$$

The node weights were normalized to the maximum node weight to obtain the normalized weights.

$$\mathbf{n}_{norm} = \frac{\mathbf{n}}{\max(\mathbf{n})} \quad (4)$$

Consistency of node weights, as defined in Sanchez-Lengeling et al. (2020), was used for evaluation of different attribution methods and model architectures.

The distribution of standard deviation for the node weights calculated using IG and InpGrad have varying attribution consistency, both across attribution methods and model architectures (Figure A.45). By visual inspection, Attentive FP - IG has the smallest mean amongst all other distributions, thus the most consistent model architecture - attribution. All further attribution analysis has been done using node weights obtained from Attentive FP - IG.

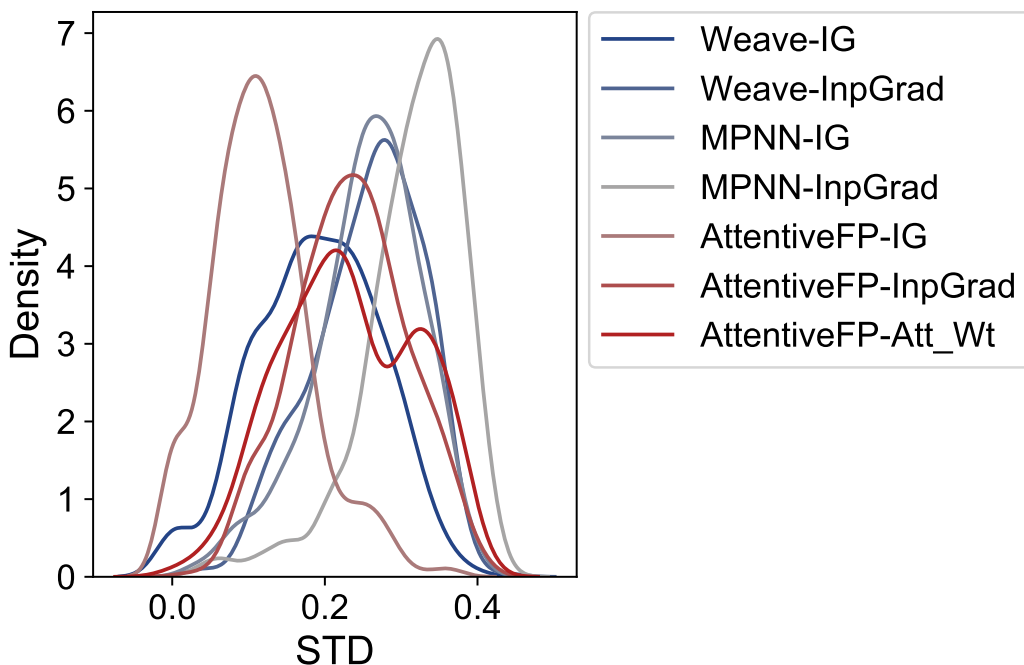


Figure A.45: Distribution of normalized node weights for different model architecture - attribution methods. Standard deviation of node weights obtained from 25 different model implementations – top 5 hyperparameter sets and 5 random seeds – were pooled across all immunogenic glycans to calculate the distribution for each model architecture and attribution combination.

Table A.7: Top monomers contributing to glycan immunogenicity, arranged in descending order of average node weight. Monomers which occur at least 20 times in the entire data set have been included in the table. The node weights have been obtained using Attentive FP – IG combination.

Monomer	Mean Node Weight
NeuNGc	0.73
Xyl	0.65
Fuc	0.65
Glc	0.64
ManNAc	0.64
Galf	0.63
NeuNAc	0.62
FucNAc	0.61
QuiNAc	0.61

H.2 VISUALIZATION OF KEY SUBSTRUCTURES

To visualize the responsible substructures in the monomers, we used \mathcal{G}_A in Equation 1, and multiplied the weights of the with the respective monomer fingerprint. This approach resulted in a weights vector with the same size as the fingerprint, with the most positively to the most negatively influencing substructure for the prediction. Using RDKit, we visualized the chemical substructures at different fingerprint indices and mapped it to the weights.

H.3 ABLATION ANALYSIS

We performed ablation analysis to check if the monomer importance or node weights changed when we assigned a zero tensor to one or more nodes (Figure A.46). For node- and monomer type-specific ablation, we observed that the importance of non-ablated nodes remained consistent.

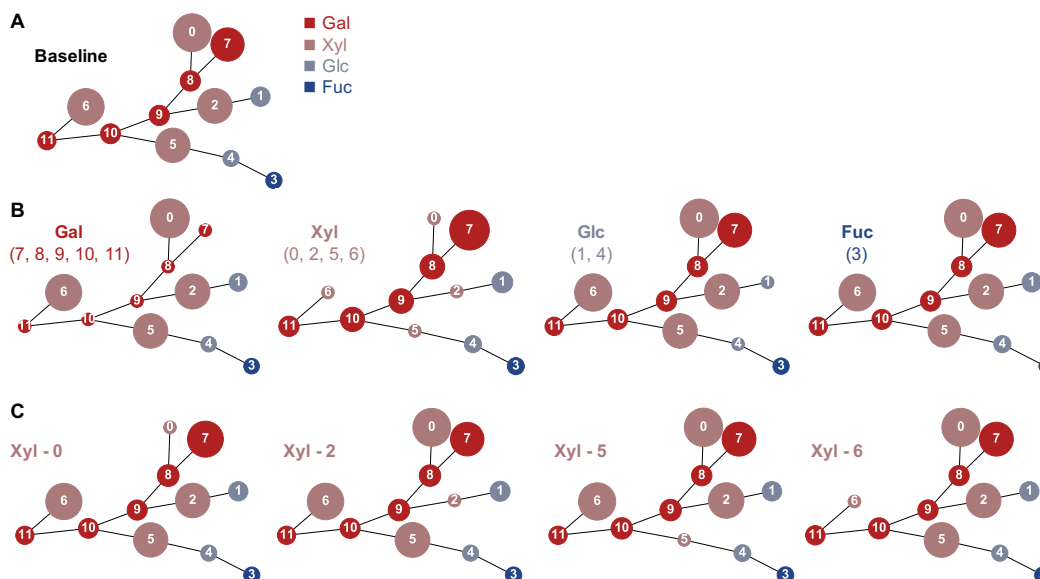


Figure A.46: Ablation analysis for immunogenic glycans shows that the importance of non-ablated monomers remains consistent, irrespective of node- and monomer-specific ablation. **A.** Glycan without any ablations is visualized as the baseline case. **B.** Monomer-specific ablation shows that ablation of a particular monomer has a negligible impact on the importance/weight of other monomers. Ablation was done by assigning zero tensors to nodes of respective monomers. This experiment was done by subsequently mutating all nodes corresponding to Gal, Xyl, Glc, and Fuc. **C.** Node-specific ablation shows that other nodes of a particular monomer have a negligible change when one of the nodes is assigned a zero tensor. This experiment was done by mutating all 4 nodes corresponding to Xyl, one at a time.

SUPPLEMENTARY TABLES

Supplementary Table 1: Validation and test metrics for the top performing sets of model hyperparameters averaged across model implementations with 5 random seeds for glycan classification, as well as test metrics averaged across 25 model implementations (5 hyperparameter sets and 5 random seeds)

Supplementary Table 2: GNN model hyperparameter sets for the top performing glycan classification models

Supplementary Table 3: Validation and test metrics for the top performing sets of model hyperparameters averaged across model implementations with 5 random seeds for peptide regression, as well as test metrics averaged across 25 model implementations (5 hyperparameter sets and 5 random seeds)

Supplementary Table 4: GNN model hyperparameter sets for the top performing peptide regression models